Expanding the Rich Crystal Chemistry of Ruthenium(V) Oxides via the Discovery of BaRu 2 O 6 , Ba 5 Ru 4 O 15 , Ba 2 Ru 3 O 10 , and Sr 2 Ru 3 O 9 (OH) by pH-Controlled Hydrothermal Synthesis

Thomas Marchandier, Quentin Jacquet, Gwenaëlle Rousse, Benoît Baptiste, Artem Abakumov, Jean-Marie Tarascon

Expanding the rich crystal chemistry of ruthenium (V) oxides via the discovery of $BaRu_2O_6$, $Ba_5Ru_4O_{15}$, $Ba_2Ru_3O_{10}$ and $Sr_2Ru_3O_9(OH)$ by pH controlled hydrothermal synthesis

Thomas Marchandier[1,2,3], Quentin Jacquet[1,2,3], Gwenaëlle Rousse[1,2,3], Benoît Baptiste[3,4], Artem M. Abakumov[5], and Jean-Marie Tarascon[1,2]

1. Collège de France, Chaire de Chimie du Solide et de l'Energie, UMR 8260, 11 place Marcelin Berthelot, 75231 Paris Cedex 05, France
2. Réseau sur le Stockage Electrochimique de l'Energie (RS2E), FR CNRS 3459, 75005 Paris, France
3. Sorbonne Université, 4 place Jussieu, F-75005 Paris, France
4. Institut de Minéralogie, de Physique des Matériaux et de Cosmochimie, CNRS, UMR 7590, 4 Place Jussieu, 75005 Paris, France
5. Center for Energy Science and Technology, Skolkovo Institute of Science and Technology, 3 Nobel Street, Moscow, 143026, Russia

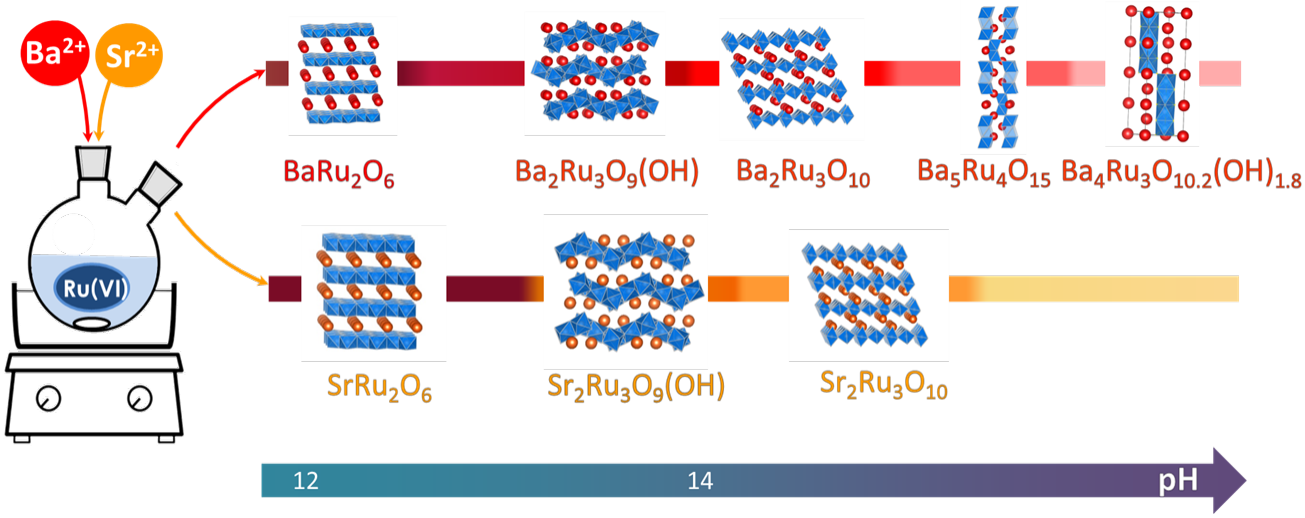

Abstract:

Along the years ruthenium oxides have been deeply investigated for their magnetic or catalytic properties. The exploration of new synthesis processes, and especially low temperature ones, is of primary importance to obtain new materials with interesting properties. Here we highlight the tunability of a low temperature (200°C) hydrothermal synthesis route of alkaline-earth ruthenates. Playing only with simple physico-chemical parameters such as pH, it is possible to obtain a large diversity of metastable compounds. Among them four compounds, namely **$BaRu_2O_6$**, **$Ba_2Ru_3O_{10}$**, **$Ba_5Ru_4O_{15}$** and **$Sr_2Ru_3O_9(OH)$**, are reported here for the first time. The influence of the reaction parameters (temperature, counter ions, reactant ratio and pH) is studied. According to these observations, the importance of the reaction pH is highlighted and a reaction scenario is proposed. Finally the crystal structures of **$Ba_2Ru_3O_{10}$**, **$Ba_5Ru_4O_{15}$** and **$Sr_2Ru_3O_9(OH)$** are reported. These findings further highlight the richness of low temperature chemistry in the discovery of new metastable phases to be further explored by physicists.

Introduction:

Ruthenium oxides are widely studied in several research fields due to their panoply of unique electrical and magnetic properties. Among them, ruthenium dioxide (RuO_2) is known to be the most efficient electrocatalyst for water splitting[1]. Besides, the binary ruthenium oxides are of prime importance. Recently, layered alkali ruthenium oxides such as Li_2RuO_3 have been used within the field of energy storage, as model insertion compounds, to unravel the electrochemical activity of the anionic framework in Li-rich layered oxides electrodes for the next generation of Li-ion batteries[2]. Among all the binary combination, alkaline-earth ruthenates are the most studied for their magnetic properties. For instance, Sr_2RuO_4 sparked considerable attention for its unconventional spin-triplet superconductivity[3] and more recently $SrRu_2O_6$ has been found to be an antiferromagnet with super-high Néel temperature (565 K)[4]. Owing to such a continuous interest, there is a need to enlarge the Ru-based oxides family members via additional chemical exploration.

Till now ruthenium-based oxides have been prepared via ceramic processes enlisting high temperature (or high pressure) to facilitate the diffusion of chemical elements in the solid state. These *modus operandi* present the advantages of reducing the number of steps, of co-reactants and allow the production of large amount of pure crystalline products with high reproducibility. Nevertheless, these drastic conditions lead solely to the thermodynamically stable compounds. In order to develop more "eco-friendly" processes and enable the synthesis of metastable phases, low-temperature processes (sol-gel, hydrothermal, co-precipitation etc…) have been developed over the last fifty years. These low temperature synthesis approaches, also referred as "chimie douce", involve multiple chemical steps as oxydoreduction, proton transfers, and/or cluster formation. Although such reactions proceed via complex nucleation-growth mechanisms, they offer many opportunities to tune the reaction pathway and obtain different materials playing with physico-chemical tools (pH, temperature, reactant ratio…). The literature is rich of elegant studies showing how the control of solvated species or reaction kinetics steps can lead to the oriented synthesis of vanadium binary oxides[5] or the polymorphic control of TiO_2[6] or FeS_2[7], to name only a few.

In light of the benefits provided by the "chimie douce", some authors have decided to implement it to the synthesis of ruthenium oxides with high ruthenium redox state (greater than IV). The hydrothermal approach with either high temperature or pressure was first tried but success had been limited[7,8,9] to the synthesis of three new metastable ruthenium(V)/alkaline-earth oxides by Hiley *et al.* in 2014 using mild temperature synthetic conditions (200°C).[10] The novelty in their approach relies in the use of a highly oxidized ruthenium salt ($KRu^{VII}O_4$) which is reduced during the reaction, rather than in the oxidation of a ruthenium precursor having a low (+IV) oxidation state as previously. Following this work

several other ruthenium (+V) phases were obtained using the same chemical trick.[11,12,13] Surprisingly, none of these studies went into a deep understanding of the reacting paths by which these new phases were formed. Progress in this direction, however, cannot be uncoupled from a deeper appreciation of the means by which the reduction and precipitation steps are affected by various physico-chemical parameters. Here we tackle this issue and use our findings to unravel new phases.

Starting from $KRu^{VII}O_4$ and alkaline-earth (M) salts ($BaCl_2$, $Sr(NO_3)_2$) we show that the modification of simple physico-chemical parameters such as reactant ratio, temperature and principally pH leads to the formation of a large diversity of metastable ruthenium(+V, +VI) binary oxides. The link between these experimental parameters and the modification of the reaction pathways is discussed as well. Among the prepared phases, the four compounds **$BaRu_2O_6$, $Ba_2Ru_3O_{10}$, $Ba_5Ru_4O_{15}$** and **$Sr_2Ru_3O_9(OH)$** have been obtained for the first time and the structure of three last ones is reported here.

Experimental Section

Synthesis

For all the synthesis described in the following sections, we used $KRuO_4$ (Alfa Aesar), $BaCl_2.2H_2O$ (Alfa Aesar), and $Sr(NO_3)_2$ (Sigma Aldrich) as sources of Ru, Ba and Sr, respectively. To prepare the aqueous alkaline solutions, extra pure KOH (>99.98 metal basis, Alfa Aesar) was used, as well as NaOH (98% Metal basis, Sigma-Aldrich) and LiOH (98% Metal basis, Alfa Aesar).

X-ray Diffraction (XRD)

Synchrotron X-ray diffraction measurements (XRD) were performed on the 11-BM beamline of the Advanced Photon source at Argonne National Laboratory, with a wavelength at 0.413 Å (the exact wavelength for each materials is given with the refinement). Laboratory powder XRD measurements were performed with a Bruker D8 Advance diffractometer operating in the Bragg-Brentano geometry at with Cu Kα radiation ($\lambda(K\alpha_1)$ = 1.54056 Å, $\lambda(K\alpha_2)$ = 1.54439 Å) and a Lynxeye XE detector. Rietveld refinements were performed using the FullProf program[14].

Single crystal X-ray diffraction (SCXRD) data were collected at the X-ray diffraction platform of IMPMC, on a Rigaku MM007HF diffractometer equipped with a RAXIS4++ image plate detector, a Mo rotating anode (λ = 0.71073 Å, Varimax multilayer optics) at 293 K. Following an equivalent procedure as described by A. Rothkirch et al., [15] the collected images were converted to the esperanto format with an in-house program (not published). Then, data reduction, cell refinement, space group determination, scaling and empirical absorption correction were performed using CrysAlisPro software(CrysAlisPro 1.171.38.46, Rigaku Oxford Diffraction, 2015).

The structure was solved using SHELXT[16] implemented in Olex2 program[17]. The refinement was then carried out with SHELXL, by full-matrix least squares minimization and difference Fourier methods. All atoms were refined with anisotropic displacement parameters.

Scanning Electronic Microscopy (SEM) and energy dispersive X-ray spectroscopy (EDX)

Scanning electronic microscopy and EDX analysis were performed using an SEM-FEG Hitachi SU-70 microscope coupled with an Oxford X-Max 50 mm^2 energy dispersive X-ray (EDX) spectrometer.

TGA analysis

Thermogravimetric analysis (TGA) was performed using a Metler Toledo TGA/DSC 3+ (LF1100°C) under argon atmosphere in order to determine the changes in sample weight with increasing temperature in order to evaluate the decomposition temperature of the different compounds synthetized. For this, a heating ramp from 25°C to 800°C was imposed, with a heating rate of 5°C per minute.

Transmission electron microscopy (TEM)

TEM sample was prepared in air by crushing the crystals in a mortar in anhydrous ethanol and depositing drops of suspension onto holey carbon grids. Electron diffraction (ED) patterns, high angle annular dark field scanning transmission electron microscopy (HAADF-STEM) images and atomic resolution EDX maps were obtained with an aberration-corrected Titan G3 electron microscope equipped with a Super-X EDX system and operated at 200 kV.

Results and discussion

1) Synthesis

As mentioned earlier the goal of this study is to investigate the hydrothermal synthesis of ruthenium oxides proposed by Hiley et al.[10] and see how it can be influenced by acting on physico-chemical parameters. The synthesis consists in reacting a ruthenium (VII) salt ($KRuO_4$) with alkaline-earth ($BaCl_2$, $Sr(NO_3)_2$) salts in aqueous alkaline hydroxides solution (KOH, NaOH or LiOH) at 200°C. Our synthesis procedure throughout this manuscript, if not otherwise mentioned, consists in i) mixing of 5 mg ($2.45x10^{-2}$ mmol) of $KRuO_4$ with the desired amount of alkaline-earth salt in 1 mL of aqueous solution of alkaline hydroxide with controlled concentration, ii) pouring the mixtures into a hermetically sealed tailor made 2 mL Teflon-lined steel autoclave and iii) placing the autoclave at 200°C in a preheated chamber furnace for 72 hours. After the reaction, powders are cleaned three times: twice with 5 mL of a 10^{-2} M solution of HCl and then with water before being dried at 100°C overnight. The resulting powder was then characterized for phase purity and composition. Hydrothermal syntheses being

known as extremely sensitive to physico-chemical parameters such as pH, reactant ratio, cations in solution or temperature, a survey of these various parameters has been undertaken.

Impact of KOH concentration and reactant ratio: speciation diagram

For guidance purpose speciation diagrams were first experimentally drawn (**Error! Reference source not found.**) as function of the KOH concentration and of the $MX_2/KRuO_4$ ratio (with MX_2 = $BaCl_2$ or $Sr(NO_3)_2$). To build these diagrams, three different molar ratios of $BaCl_2/KRuO_4$ reactants (0.5, 1 and 2) were studied. For each of these ratios, nine concentrations of KOH ranging from 0 to 8 $mol.L^{-1}$ were considered. The same ratios were used for $Sr(NO_3)_2/KRuO_4$, with seven concentrations of KOH ranging from 0 to 3 $mol.L^{-1}$. We observed that the higher KOH concentration is, the lower the amount of powder is formed at the end of the reaction (after 72 hours) and this also depends on the nature of alkaline earth cation. As a consequence, no KOH] concentration greater than 8 M and 3 M will be studied from now on for the barium/ruthenium and strontium/ruthenium systems, respectively. The resulting samples from such a survey that correspond to symbols in the diagram (Figure 1) were analysed for phase purity by XRD and single phase domains are defined by different colours. For multiphase samples, the relative ratios are not given, as they slightly fluctuate from one experiment to the other.

For the barium/ruthenium system with a $BaCl_2/KRuO_4$ ratio of 1 we observed the formation of five phases (**Error! Reference source not found.**a) upon increasing KOH concentration: **$BaRu_2O_6$** ([KOH]<1M), **$Ba_2Ru_3O_9(OH)$** (1M<[KOH]<4M), **$Ba_2Ru_3O_{10}$** (4M<[KOH]<6M), **10H-$Ba_5Ru_4O_{15}$** (6M<[KOH]<7M), and finally the layered perovskite **$Ba_4Ru_3O_{10.2}(OH)_{1.8}$** for [KOH] > 7M. Note that **$BaRu_2O_6$**, **$Ba_2Ru_3O_{10}$** and **10H-$Ba_5Ru_4O_{15}$** are new phases obtained in pure form except for **10H-$Ba_5Ru_4O_{15}$** which was contaminated with traces of either **$Ba_2Ru_3O_{10}$** or **$Ba_4Ru_3O_{10.2}(OH)_{1.8}$**. This contrasts with the strontium/ruthenium system with $Sr(NO_3)_2/KRuO_4$ of 1 for which we solely found (**Error! Reference source not found.**) three different phases which are in the order of increasing the KOH concentration : **$SrRu_2O_6$**, **$Sr_2Ru_3O_9(OH)$** and **$Sr_2Ru_3O_{10}$,** respectively. Interestingly, none of the isolated phase have the same M/Ru ratio whatever the alkaline earth cation (M = Ba or Sr). Moreover, this ratio is not distributed randomly within the diagram but increases with the KOH concentration taking the values of 0.5, 0.66, 1.1, 1.25, 1.3 for **$BaRu_2O_6$**, **$Ba_2Ru_3O_9(OH)$**, **$Ba_4Ru_3O_{10.2}(OH)_{1.8}$**, **10H-$Ba_5Ru_4O_{15}$**, **$Ba_4Ru_3O_{10.2}(OH)_{1.8}$**. The same trend applies as well for the strontium/ruthenium system and this is not fortuitous as discussed latter.

Our results further indicate that the M/Ru ratio in the obtained phases greatly differs from the reactant ratio. Nevertheless, the fact remains that this reactant ratio impacts considerably the domain of OH concentrations, that is the pH, over which these phases are forming as shown in Figure 1a and

Figure 1b. For example, when the reactants are alkaline-earth rich ($MX_2/KRuO_4$ >1), phases richer in alkaline earth are formed in a broader [KOH] range (red and orange colours), while such phases cannot even form when the reactants are alkaline-earth poor. The inverse observation is made with alkaline-earth poor reactants (i.e $MX_2/KRuO_4$ <1) (see green and blue domains **Error! Reference source not found.**a).

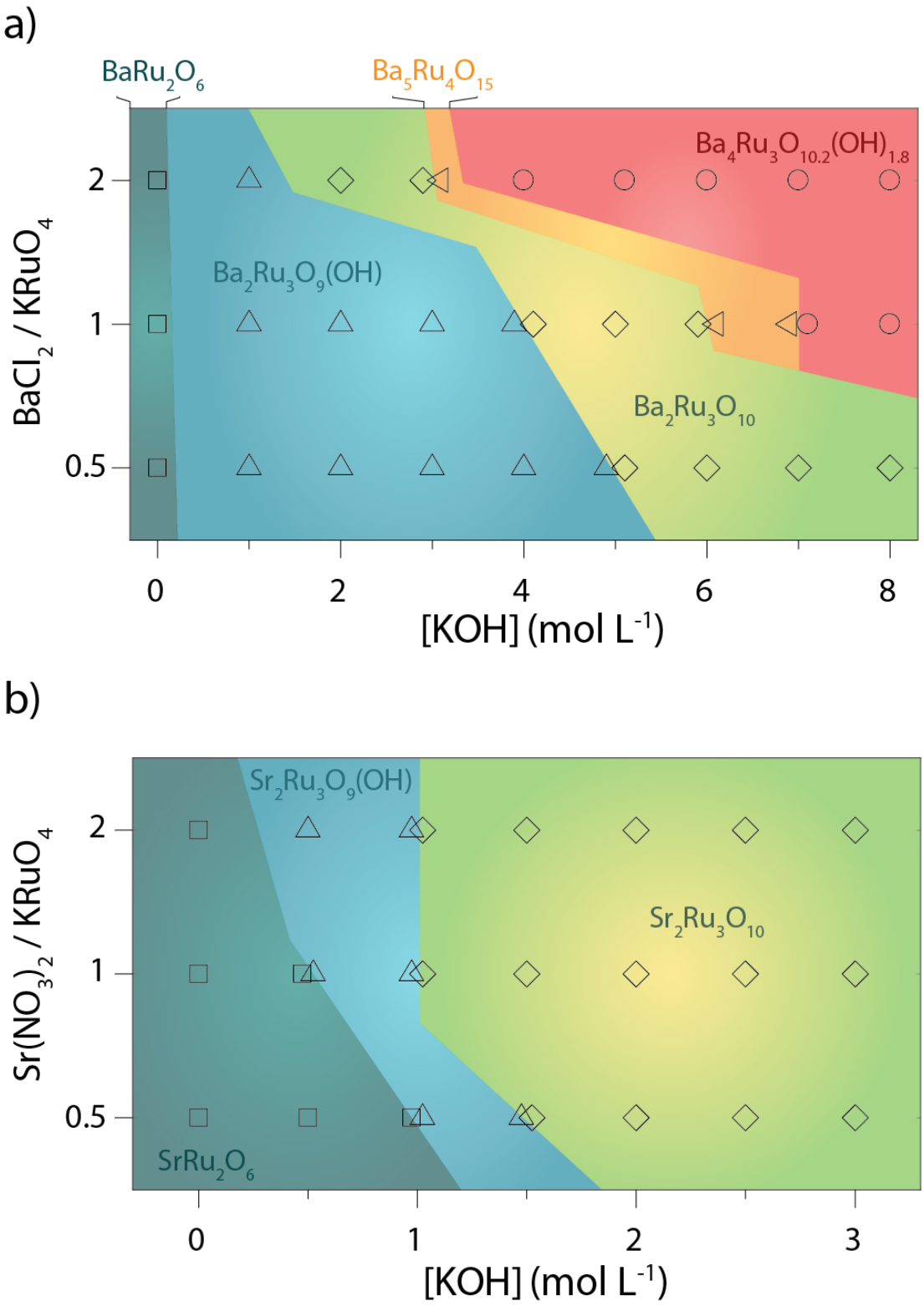

Figure 1: Speciation diagram of ruthenium oxides as a function of the initial KOH concentration and reactant molar ratios. a) Speciation diagram of the ruthenium/barium system, symbols correspond to experimental points: $BaRu_2O_6$ (□), $Ba_2Ru_3O_9(OH)$ (△), $Ba_2Ru_3O_{10}$ (◇), 10H-$Ba_5Ru_4O_{15}$ (◁), $Ba_4Ru_3O_{10.2}(OH)_{1.8}$ (◯).b) Speciation diagram of the ruthenium/strontium system, symbols correspond to experimental points: $SrRu_2O_6$ (□), $Sr_2Ru_3O_9(OH)$ (△), $Sr_2Ru_3O_{10}$ (◇). Colored areas are a visual help for the reader to apprehend the domains of formation for each compound.

Impact of the counter cation

Having explored the impact of KOH concentration on the nature of the synthesis products within the Ba-Ru and Sr-Ru systems, we next check the importance of the nature of counter cation (K^+). New syntheses were performed by replacing KOH by NaOH and LiOH while keeping $BaCl_2/KRuO_4$ and $Sr(NO_3)_2/KRuO_4$ precursor ratios of 1. For the strontium/ruthenium couple, whatever the alkaline hydroxides used, the obtained phases remain the same. This is not any longer true in presence of the barium/ruthenium couple for hydroxides concentrations greater than 1M since with NaOH and LiOH, we obtained the **$NaBa_4Ru_3O_{12}$** and **$LiBa_4Ru_3O_{12}$** phases, respectively as opposed to **$Ba_2Ru_3O_{10}$, 10H-$Ba_5Ru_4O_{15}$** and **$Ba_4Ru_3O_{10.2}(OH)_{1.2}$** for [KOH] > 1 M, as previously described. Let's recall that the aforementioned Li and Na-based compounds are not new since they have been previously reported using ceramic high temperature process (800°C). For completeness we also examined the influence of counter ion concentration, replacing KOH with KCl. Whatever the added KCl concentration we only obtained $BaRu_2O_6$. Therefore, the hydroxide ions are essential to guide the reaction. Altogether these results show that the hydroxide counter ions can modify the speciation diagram leading to new compounds in which they could become a component of the structure.

Impact of the temperature

Temperature is another parameter that we have investigated as it is of paramount importance in controlling reaction pathways. Figure 2 represents XRD patterns of the phases resulting from heating precursor mixtures ($BaCl_2$:$KRuO_4$ = 1:1 at [KOH] = 4 M) at four different temperatures ranging from 120°C to 220°C. Crystalline phase are solely obtained for T > 120°C. The phase formed at 175°C (red diamonds) can easily be identified as **$Ba_2Ru_3O_{10}$**. With increasing temperature to 200°C, there is the appearance of a second phase **$Ba_2Ru_3O_9(OH)$** (blue triangles) which grows at the expense of the first one and becomes single phase as the temperature reaches 220°C. This indicates a well pronounced influence of the temperature on the speciation diagrams and may explain, based on the temperature inhomogeneity of our furnaces, the occasional irreproducibility of the synthesis.

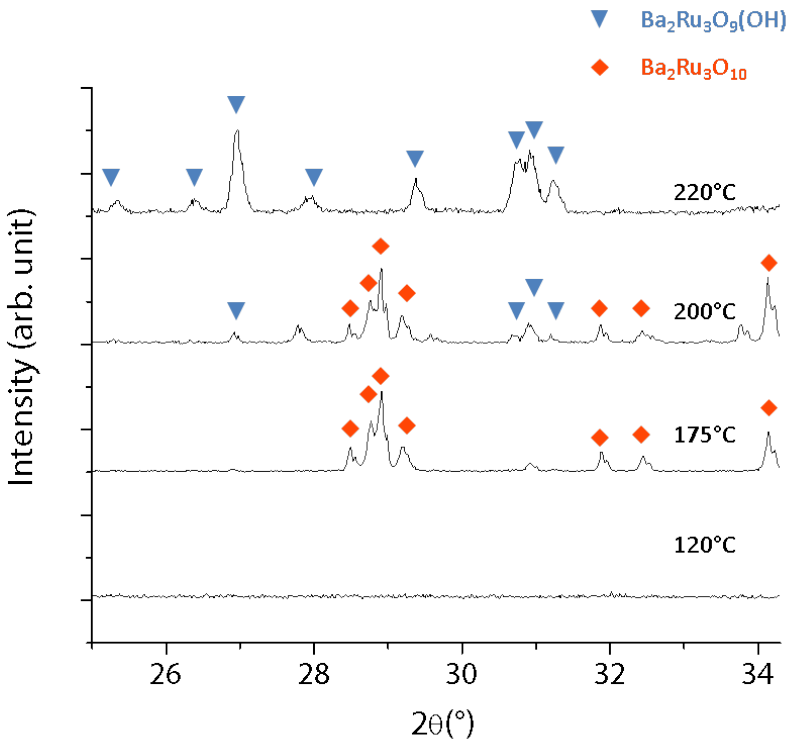

Figure 2: X-ray diffraction patterns of powders obtained at different temperatures using $BaCl_2$:$KRuO_4$ = 1:1 at [KOH] = 4 M. Blue triangles represent $Ba_2Ru_3O_9(OH)$ peaks whereas red d represent $Ba_2Ru_3O_{10}$ peaks.

Overall, we have shown that the low temperature solution process leading to the formation of new Ru-based binary oxides is sensitive to many parameters, namely, reactant ratio/concentration, temperature and particularly pH. Interestingly, we experienced a positive synergetic effect between the various parameters for synthesising pure phases as opposed to contaminated phases by acting on a single parameter. For instance, by acting on the pH alone the obtained **$BaRu_2O_6$,** and **10H-$Ba_5Ru_4O_{15}$** are always contaminated by minute amounts of RuO_2, **$Ba_2Ru_3O_{10}$** and **$Ba_4Ru_3O_{10.2}(OH)_{1.2}$**. This synergetic effect is a gift for preparing new phases but a nightmare when attempt to rationalize the synthetic process as described next.

2) Mechanism investigations

A grasp to understand such reaction can be provided by considering reactant and products and using the guidance from the Pourbaix diagram (**Error! Reference source not found.**a). It indicates that, using the synthesis concentrations described above, $KRuO_4$, dissolved into K^+ and RuO_4^-, is reduced by water to form water stable $Ru^{VI+}O_4^{2-}$ species. According to the redox state of the final compound obtained (+V or +VI), this implies that RuO_4^{2-} is then reduced by water from its +VI to +V oxidation state. Using these simple deductions, one can write the global reaction equations for the formation of the different compounds:

$$RuO_4^{2-} + \frac{1}{2}Ba^{2+} + \frac{1}{2}H_2O = \frac{1}{2}\mathbf{BaRu_2O_6} + HO^- + \frac{1}{4}O_2 \qquad (eq\ 1)$$

$$RuO_4^{2-} + \frac{2}{3}Ba^{2+} + \frac{1}{2}H_2O = \frac{1}{3}\mathbf{Ba_2Ru_3O_9(OH)} + \frac{2}{3}HO^- + \frac{1}{4}O_2 \qquad (eq\ 2)$$

$$RuO_4^{2-} + \frac{2}{3}Ba^{2+} + \frac{1}{3}H_2O = \frac{1}{3}\mathbf{Ba_2Ru_3O_{10}} + \frac{2}{3}HO^- + \frac{1}{6}O_2 \qquad (eq\ 3)$$

$$RuO_4^{2-} + \frac{5}{4}Ba^{2+} + \frac{1}{2}HO^- = \frac{1}{4}\mathbf{Ba_5Ru_4O_{15}} + \frac{1}{4}H_2O + \frac{1}{4}O_2 \qquad (eq\ 4)$$

$$RuO_4^{2-} + \frac{4}{3}Ba^{2+} + \frac{2}{3}HO^- = \frac{1}{3}\mathbf{Ba_4Ru_3O_{10.2}(OH)_{1.8}} + \frac{1}{30}H_2O + \frac{19}{60}O_2 \qquad (eq\ 5)$$

Postulating that these reactions are equilibrium one can write the equilibrium constant associated using the general formula:

$$K = \frac{[HO^-]^a {P_{O_2}}^c}{[RuO_4^{2-}][Ba^{2+}]^b}$$

Where a, b and c depend on the compound formed, and a is positive (eq 1 to 3) or negative (eq 4 and 5) depending on the reaction (for instance a = 1, b = 0.5 and c = 0.25 for $BaRu_2O_6$). According to these simple equations, the influence of the reactant ratio and the hydroxide concentration is highlighted. Indeed, structures associated with small *a* values (in particular for negative ones) would be more favorised at higher hydroxide concentration. Identically, phase for which *b* is high would be more favorised at high [Ba^{2+}] values. This result is consistent with the experimental speciation diagram drawn in Figure 1 as it predicts the order of appearance of the different materials with pH. For instance, **$BaRu_2O_6$** associated to the larger a value (*a*=1) is formed at the lowest [OH^-] whereas **$Ba_4Ru_3O_{10.2}(OH)_{1.8}$**, associated to the smallest *a* (*a*= -0.66) is formed for the highest hydroxide concentration. It is important to note, that this simple reasoning doesn't take into account free energy of formation of solid phase which would be essential to simulate a rigorous phase diagram.

This thermodynamic approach is based on the assumption that all the equations written above are equilibrium. It should then be possible to transform one phase to another playing with [OH^-] and/or [Ba^{2+}]. For instance **$BaRu_2O_6$** should be changed into $Ba_2Ru_3O_{10}$ according to:

$$\boldsymbol{BaRu_2O_6} + \frac{1}{3}Ba^{2+} + \frac{2}{3}HO^- + \frac{1}{6}O_2 = \frac{\mathbf{2}}{\mathbf{3}}\boldsymbol{Ba_2Ru_3O_{10}} + \frac{1}{3}H_2O$$

To investigate this point **$BaRu_2O_6$** was heated at 200°C in 5 M [OH^-] with 0.1 M Ba^{2+}. After 5 days of reaction the solution turned orange (characteristic to the presence of RuO_4^{2-} in solution) and **$Ba_2Ru_3O_{10}$** and **10H-$Ba_5Ru_4O_{15}$** are formed. These observations are perfectly consistent with a thermodynamic scenario, as **$BaRu_2O_6$** is supposed to dissolve into RuO_4^{2-} according to the equations above, and the

formation of the two phases at this hydroxide concentration is in line with the speciation diagram described in Figure 1. However, the presence of RuO_4^{2-} in solution necessitates the oxidation of the ruthenium specie, the implication of dissolved oxygen to do it is doubtful as the experiment has been reproduced bulling argon in the autoclave before heating and it led to the same results. A disproportionation of Ru(V) can be then suggested following:

$$BaRu_2O_6 \rightarrow RuO_2 + \mathrm{RuO_4^{2-}} + \mathrm{Ba^{2+}}$$

No RuO_2 has been clearly seen on XRD pattern but amorphous phase is likely. This prevents to go from one phase to another just playing with pH.

Nevertheless, as mentioned in the synthesis part, we observed that increasing [OH-] results in lowering the amount of powder formed at the end of the reaction (after 72 hours). This observation can be proved considering the concentration of $[RuO_4^{2-}]$ at the end of the reaction. Solutions of this anion are deep orange, we can observe that for low $[OH^-]$ the final solutions are colourless, indicating that all $[RuO_4^{2-}]$ is consumed whereas at higher $[OH^-]$ final solution remain deep orange. This result contradicts the pure thermodynamic scenario as the equilibrium constant predicts (with a being negative) that the higher $[OH^-]$ is the lower $[RuO_4^{2-}]$ should be. This result let think that kinetic could be implied in this reaction as well, especially, it seems that hydroxides slow down the global reaction rate. Moreover, one can argue that the equilibrium constant of formation of **$Ba_2Ru_3O_9(OH)$** and **$Ba_2Ru_3O_{10}$** are identically impacted by $[OH^-]$ as a is identical for both (a=2/3). However these phases are formed in distinct pH domains, which is in contradiction with the pure thermodynamic scenario. In this case, the role of reaction kinetics has probably to be taken into account.

Finally, the experimental speciation diagrams can mostly be rationalized using a simple thermodynamic approach, however the engagement of reaction kinetics is proved in this system. Understanding the precise impact of $[OH^-]$ on reaction kinetics deals with mechanism investigation. A likely scenario consists in two steps that enlist first the thermal reduction in solution of Ru(VI) into an hypothetic Ru(V) entity and then the precipitation of this entity with alkaline-earth cations. The implication of hydroxide concentration in one of this step could explain the observations described above. Better understanding of the different steps implied in the process is primordial to fully understand the hydrothermal process and then to obtain other new phases.

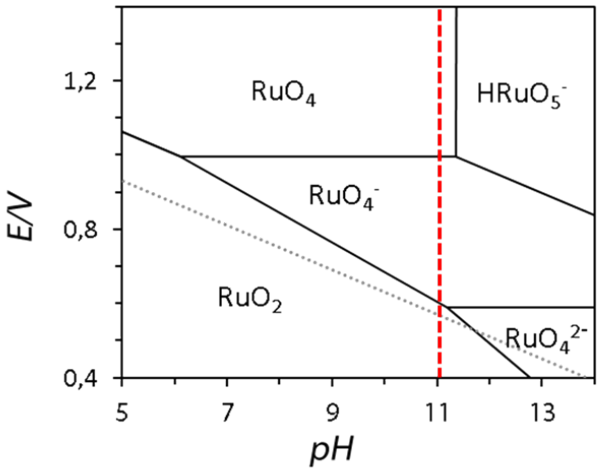

Figure 3: Reduced Pourbaix diagram of Ruthenium/H_2O for [Ru] = 10^{-2} mol.L^{-1}. This diagram was built using data found in reference [18]. Grey dotted line represents the water oxidation line. The red dotted line represents the pH obtained after the dissolution of $KRuO_4$ in the reaction concentrations.

Structural Characterization

The crystal structures of newly synthesized **10H-$Ba_5Ru_4O_{15}$**, **$Ba_2Ru_3O_{10}$** and **$Sr_2Ru_3O_9(OH)$** were determined. Although **$BaRu_2O_6$** is also a new phase, its detailed structural characterization will be reported elsewhere. For sake of clarity, we will handle each compound separately by first reporting the exact synthesis process of the powders used for carrying the structural determination.

a) Structure of 10H-$Ba_5Ru_4O_{15}$

About 100 mg of pure **10H-$Ba_5Ru_4O_{15}$** was obtained by mixing $KRuO_4$ with BaO_2 (1:2 molar ratio) with 1 mL of distilled water in a 10 mL silicon carbide vessel, which was subsequently heated to 200°C in three minutes and hold at 200°C for three hours in a microwave oven. To wash the powder, the protocol described in the synthesis part is used. Note that caution has to be taken with acidic conditions, as the material deteriorates within 10 to 20 minutes in 1 M HCl.

The synchrotron powder XRD pattern of the resulting powder is plotted in Figure 6. At a first glance, it is very similar to what was observed by Ogawa et al[19] for 10H-$BaRuO_3$ (where H refers to the hexagonal symmetry of underlying close packing of the BaO_3 layers). However, the pattern can be indexed with the $P6_3/mmc$ space group and lattice parameters a = 5.792187(14) Å and c = 23.53579(16) Å, which are noticeably different from the unit cell parameters of 10H-$BaRuO_3$ (a = 5.756(2) Å, c = 23.727(8) Å). Moreover, the Rietveld refinement using the structural model for 10H-$BaRuO_3$ leads to inappropriate intensities for some reflections. These two observations indicate that our synthesized compound differs from 10H-$BaRuO_3$. The refinement can indeed be greatly improved by introducing vacancies at the Ru1 site, as shown in Figure S3, and is in agreement with the possibility of Ru vacancies that was

suggested by Ogawa from single crystal structure investigations.[19] In our case, the chemical composition, obtained after refinement of the Ru1 occupancy, corresponds to the $BaRu_{0.88}O_3$ formula (Table S 1). However, despite improving the refinement, this model does not take into account the pronounced asymmetry on the main (110) reflection. This indicates the presence of microstructural defects such as stacking faults. The 10H-$BaRuO_3$ ideal structure consists of a $(chhch)_2$ stacking of close-packed BaO_3 hexagonal layers along the c-direction, where "*h*" and "*c*" stand for the "hexagonal" (i.e. occuring in the *hcp* ...ABAB... structure) and "cubic" (i.e. occuring in the fcc ...ABC... structure) layers, respectively. The ruthenium cations occupy interstitial octahedral sites leading to alternate face-sharing $Ru_2\square O_{12}$ ($\square$ - Ru vacancy) trimers and Ru_2O_9 dimers, where face-sharing occurs at the "*h*"-type close-packed layers (**Error! Reference source not found.**a). In our case, the asymmetry of the (001) peak and the clear presence of Ru vacancies on the central octahedron in the $Ru_2\square O_{12}$ trimers encouraged us to explore 10H-$BaRu_{0.88}O_3$ at a local scale using electron diffraction (ED) patterns, high angle annular dark field scanning transmission electron microscopy (HAADF-STEM) images and atomic resolution energy dispersive X-ray maps.

The [001] ED pattern of $BaRu_{0.88}O_3$ (Fig. S4) is in good agreement with the close-packed structure of the BaO_3 layers. The [-120] and [-110] ED patterns, showing the *h*0*l* and *hhl* reciprocal lattice rows, demonstrate that the stacking sequence of the BaO_3 layers is faulted. The reflection sequence associated with the 10H structure of $BaRu_{0.88}O_3$ with the *c* parameter of ~23.5 Å is present (marked with brackets in Fig. S4), but always together with other reflections corresponding to different stacking periodicities. HAADF-STEM image of the 10H $(chhch)_2$ stacking sequence clearly demonstrates that the material is Ru-deficient and the Ru vacancies are located in the mid octahedron of the $Ru_2\square O_{12}$ trimers (Figure 4b). However, profiling the HAADF intensity along the $Ru_2\square O_{12}$ trimers shows that the central octahedron is not always vacant and sometimes can be randomly populated with the adjacent Ru cations (Figure 4c). Interestingly, this Ru cation does not sit at the center of the mid octahedron being shifted towards either the first of the third octahedron of the trimer by ~0.35 Å. The HAADF-STEM image in Figure 5b sheds light on the most abundant stacking faults showing thin lamella of the 4H $(ch)_2$ stacking sequence embedded into the 10H $(chhch)_2$ matrix. This lamella in fact corresponds to the 4H-$BaRuO_3$ structure (has already been reported[20]) forming a coherent intergrowth with the 10H-$BaRu_{0.88}O_3$ structure. Additionally, the assignment of the atomic columns has been confirmed with the atomic resolution EDX mapping at the interface between 4H-$BaRuO_3$ and 10H-$Ba_5Ru_{5-x}O_{15}$ (Fig. S5).

To the best of our knowledge, it is the first time that a **10H-$Ba_5Ru_4O_{15}$** compound is reported, but unfortunately our trials to obtain it without any 4H-$BaRuO_3$ domains failed, whatever the synthesis conditions we tried. This highlights the ability of such structures to accommodate stacking faults.

To complete the structural study on this material and according to the TEM results, the effect of introducing 4H-$BaRuO_3$ stacking faults on the 10H-$Ba_5Ru_4O_{15}$ XRD pattern was studied. Using the

FAULTS program,[21] one can indeed create structures built on two different sequences of layers (in our case 10H-$Ba_5Ru_4O_{15}$ and 4H-$BaRuO_3$), and one can define between these layers one or several stacking vectors, each one being associated with a stacking probability (P). With this approach, one can simulate a pure 4H-$BaRuO_3$ structure with stacking probabilities $P_{10H\rightarrow4H} = 1$ and $P_{4H\rightarrow10H} = 0$. Identically, a pure 10H-$Ba_5Ru_4O_{15}$ can be obtained with $P_{10H\rightarrow4H} = 0$ and $P_{4H\rightarrow10H} = 1$. In our case, we have considered all possibilities in between with the additional constraint that $P_{10H\rightarrow10H} = 1 - P_{4H\rightarrow4H} = P$, that corresponds of having no correlation between two successive layers. XRD patterns were simulated varying P from 1 (which correspond to pure 10H-$Ba_5Ru_4O_{15}$) to 0 (which correspond to pure 4H-$BaRuO_3$ layers) and are compared against the experimental XRD pattern on **Error! Reference source not found.**. These simulations show large differences in peak intensities, peak shapes and peak positions, even if P is only slightly modified. Our experimental XRD pattern looks close to the pattern simulated for P = 0.9, and this value was used as a starting point for the refinement of our synchrotron pattern using FAULTS. The results of the refinement is presented in Figure 7 and shows an improvement compared to the Rietveld refinement previously discussed (Figure S3); it leads to a stacking probability of 91(2)%, which indicates that the 4H-$BaRuO_3$ interlayers occupy 9(2)% of the 10H-$Ba_5Ru_4O_{15}$ structure. This example shows the importance of taking into account stacking faults, especially if the intergrowth layers have a different stoichiometry than the host structure.

Finally this **10H-$Ba_5Ru_4O_{15}$** compound is different from 10H-$BaRuO_3$ reported previously.[19] As previously mentioned, lattice parameters are different (maybe resulting from the different Ru content), and moreover, **10H-$Ba_5Ru_4O_{15}$** presents Ru in the +V oxidation state while it is Ru(IV) for 10H-$BaRuO_3$. Lastly, for sake of completion, TGA analysis indicates that **10H-$Ba_5Ru_4O_{15}$** is stable till 500°C, prior to decompose in mainly $BaRuO_3$ (Figure S7).

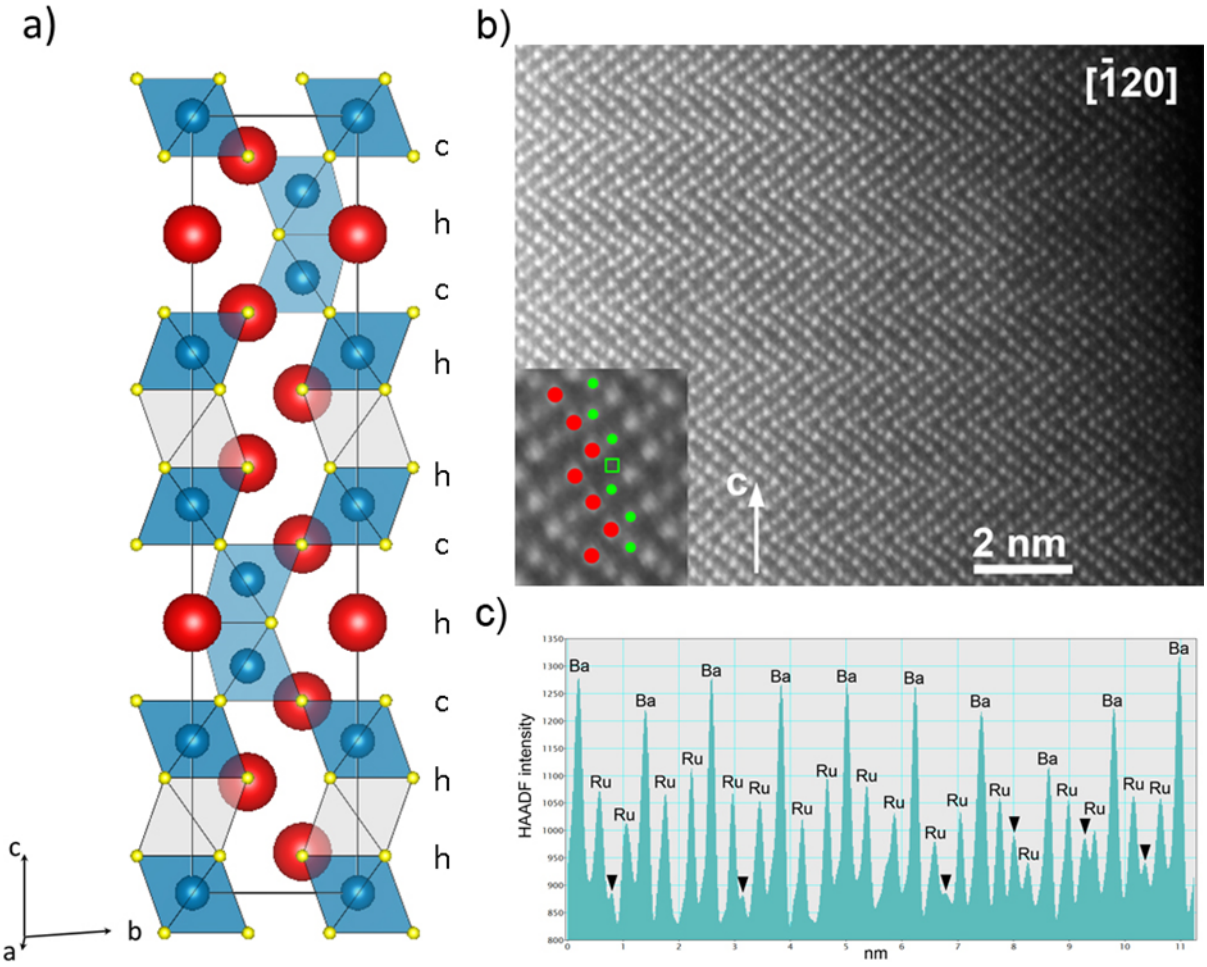

Figure 4 : a) The structure of $Ba_5Ru_4O_{15}$ viewed along the *a* direction. Ba atoms are in red and RuO_6 octahedra are in blue with Ru atoms in blue and O atoms in yellow, grey octahedron represents the vacant octahedral sites. Stacking type is given on the right. b) [-120] HAADF-STEM image of the 10H-$Ba_5Ru_4O_{15}$ structure showing the assignment of the Ba (red) and Ru (green) atomic columns. The Ru vacancy is denoted with a green square. c) HAADF intensity profile along the $Ru_2\square O_{12}$ trimers. Note variable intensity at the place of the vacant octahedron (black arrowheads) indicating its random population with Ru cation and vacancy. The Ru cations are randomly shifted from the centers of these octahedra

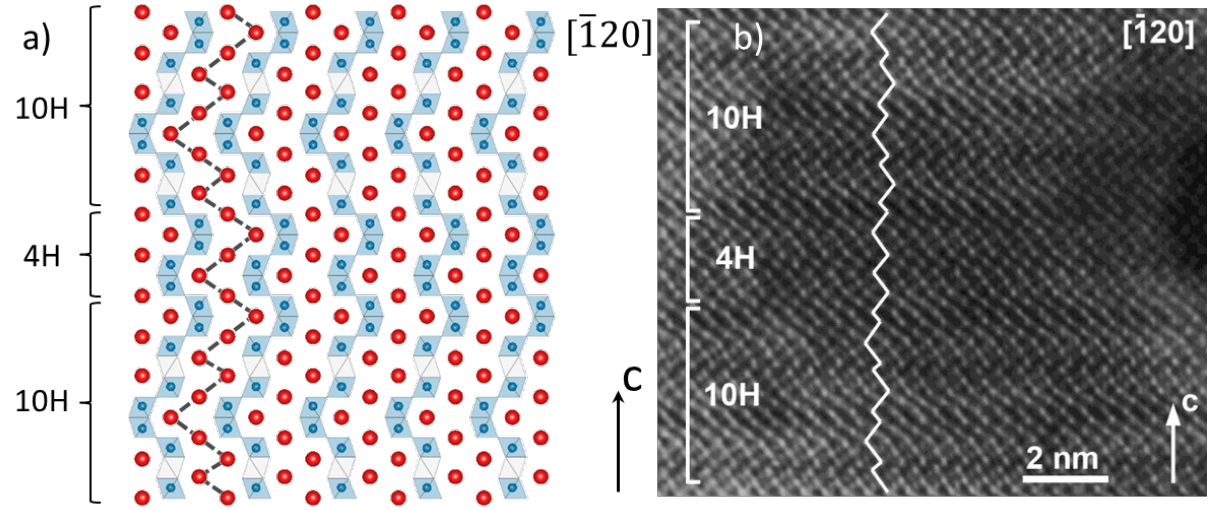

Figure 5: a) Representation of the stacking faults, in the **10H-$Ba_5Ru_4O_{15}$** seen from the [-120] direction, Ba atoms are in red and RuO_6 octahedrons are in blue. The black dotted line shows the sequence of BaO_3 layer. b) [-120] HAADF-STEM image

showing thin lamella of 4H (ch)2 stacking in the 10H (chhch)2. The sequence of the BaO_3 layers is traced with the white zig-zag line, where the kinks stand for the h-type layers

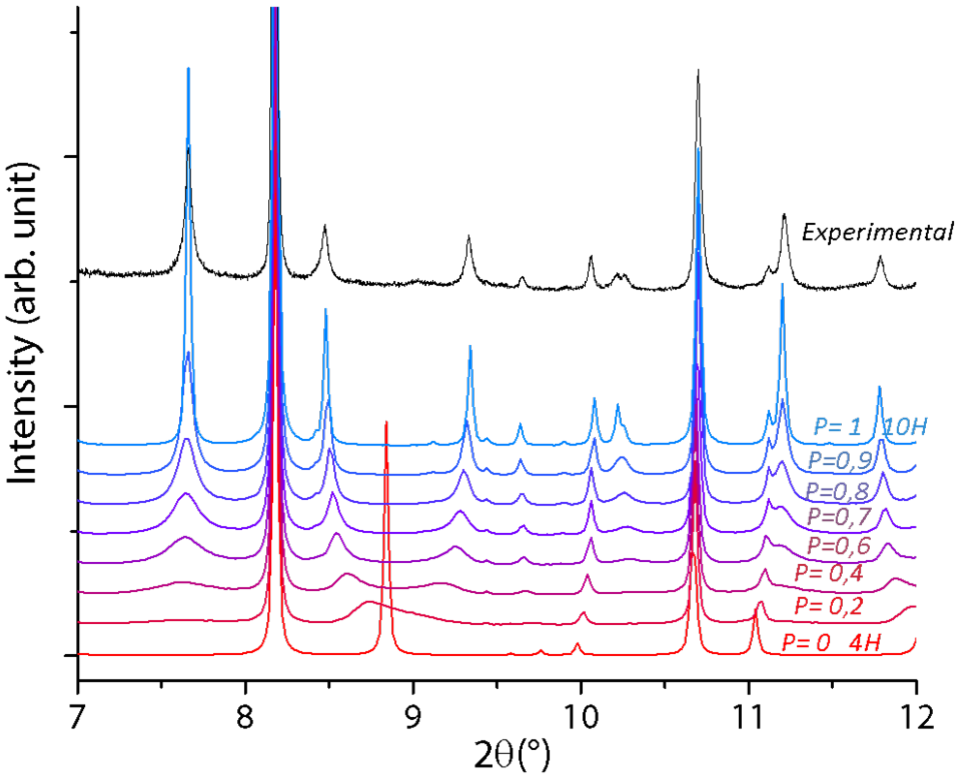

Figure 6: Comparison between experimental synchrotron XRD pattern (top black line) and simulated XRD patterns of 10H-$Ba_5Ru_4O_{15}$ with 4H-$BaRuO_3$ stacking faults, using different 4H to 10H stacking probabilities (P), from pure 4H-$BaRuO_3$ (P = 0) to pure 10H-$Ba_5Ru_4O_{15}$ (P = 1).

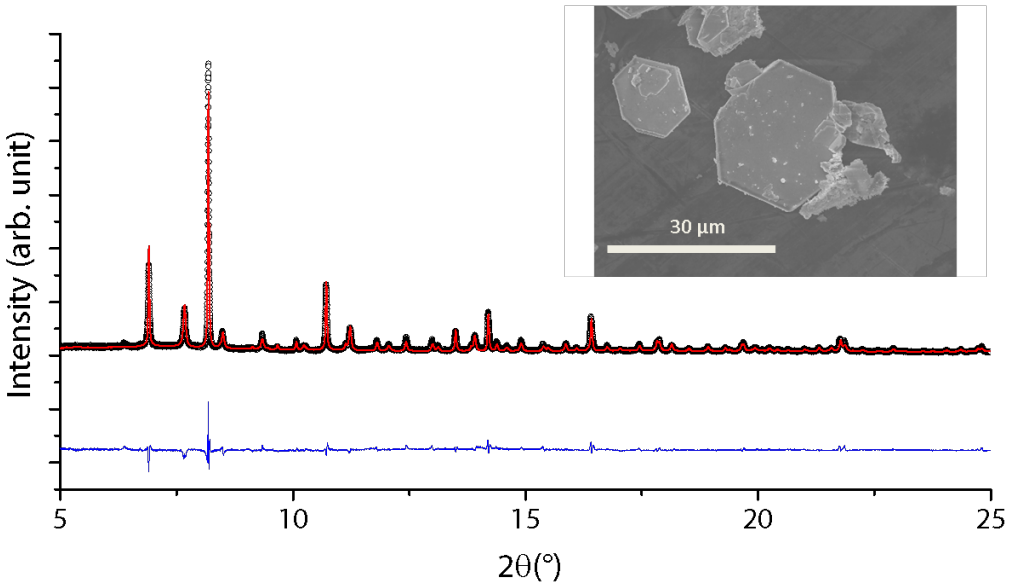

Figure 7: Refinement of synchrotron X-ray diffraction patterns of 10H-$Ba_5Ru_4O_{15}$ (λ= 0.412763 Å) using the FAULTS program. The black circles, red continuous line, and bottom blue line represent the observed, calculated, and difference patterns, respectively. Insert: SEM picture of 10H-$Ba_5Ru_4O_{15}$ crystals.

b) Structure of $Ba_2Ru_3O_{10}$

Pure **$Ba_2Ru_3O_{10}$** powder was obtained by scaling up the process described in the synthesis part. In a 20 mL Teflon-lined steel autoclave, 50 mg of $KRuO_4$, 59.8 mg of $BaCl_2.2H_2O$ (1:1 molar ratio) are mixed in 10 mL of 5 M KOH aqueous solution and heated to 200°C in a preheated fan oven for 72 hours. The powder is then washed using the protocol described in the synthesis part. SEM micrographs show the formation of rectangular facetted micrometer-sized platelets (Figure 8). At this stage it is worth to recall that the counterpart strontium **$Sr_2Ru_3O_{10}$** phase has been previously obtained impure using high temperature and pressure hydrothermal synthesis (480–650°C, 1800–2100 bars)[8] (the synthesis of pure $Sr_2Ru_3O_{10}$ and structural information can be found in the SI).

The powder X-ray synchrotron diffraction pattern of **$Ba_2Ru_3O_{10}$** was indexed using the DICVOL program[22,23] in a monoclinic unit cell with the following lattice parameters *a* = 11.45979 Å, *b* = 5.80123 Å, *c* = 6.50785 Å, β = 105.44° (Vol =418.005 Å^3). These results coupled with the EDX measurements (which indicated Sr/Ru = 2/3 ratio) lead us considering $Sr_2Ru_3O_{10}$ as initial structural model, and replacing Sr with Ba. Positions of all atoms were then refined using the Rietveld method. The refinement showed in **Error! Reference source not found.** presents good reliability parameters (χ^2 = 4.08 and R_{Bragg} = 4.87%) and structural parameters are gathered in **Error! Reference source not found.**. The crystal structure is presented in Figure 9. Ruthenium atoms are found in two different Wyckoff sites and are octahedrally coordinated by oxygen atoms. Ru(2)O_6 octahedra share edges to form chains running along [010], and these chains are connected one to each other by Ru(1)O_6 octahedra through corners. This creates Ru layers stacked along [100]. Barium atoms are located in the interlayer space and coordinated to nine oxygen atoms. Bond valence calculations show different redox states for the two crystallographic sites of ruthenium: 5.4 for the 4*h* site (Ru2) and 5.1 for the 2*a* site (Ru1). This leads to an average oxidation state of 5.3+, in full agreement with the one expected from the charge neutrality (5.33+). Lastly, we explored the stability of this compound by TGA. According to it, mass loss is observed around 500°C (Figure S8). This is confirmed by ex-situ X-ray diffraction which shows that this phase decomposes into RuO_2 and $BaRuO_3$ above 500°C.

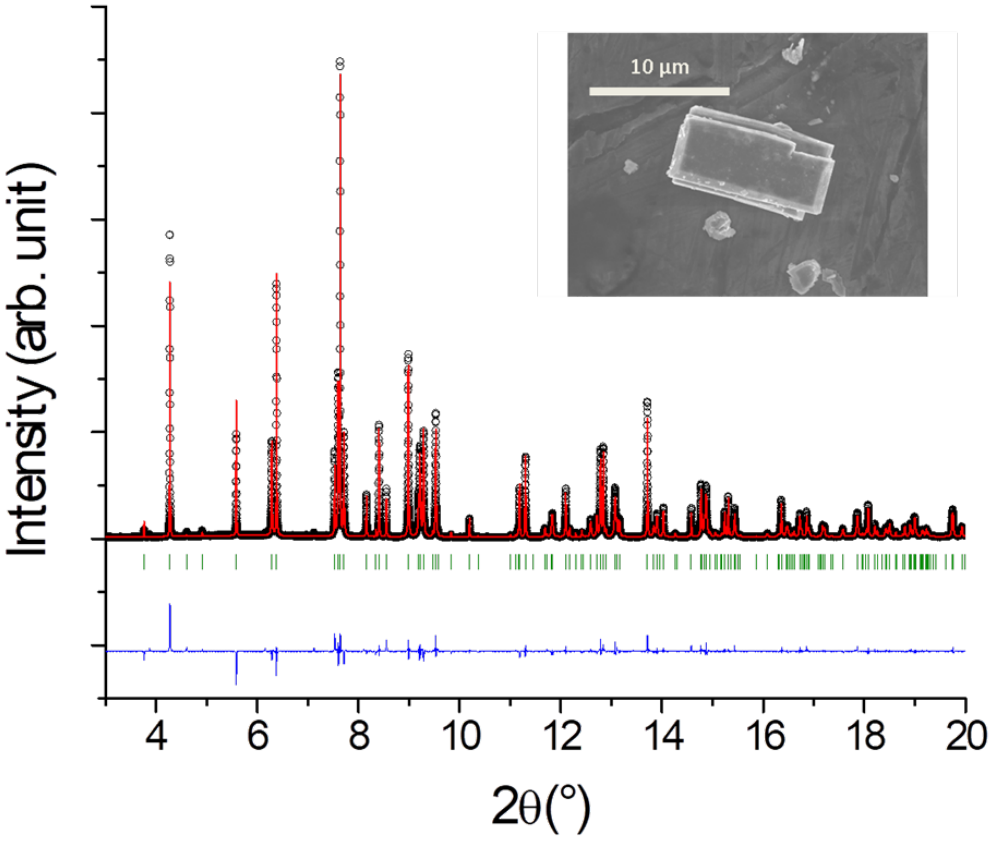

Figure 8: Rietveld refinement of synchrotron X-ray diffraction patterns of $Ba_2Ru_3O_{10}$ (λ= 0.412763 Å). The black circles, red continuous line, and bottom blue line represent the observed, calculated, and difference patterns, respectively. Vertical green tick bars are the Bragg positions. Insert: SEM picture of $Ba_2Ru_3O_{10}$ crystals

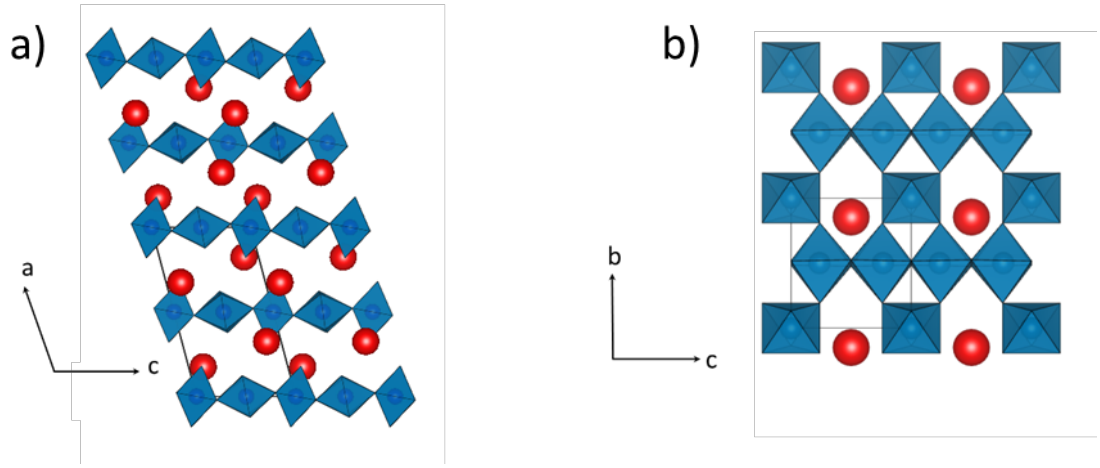

Figure 9: The structure of $Ba_2Ru_3O_{10}$ Ba atoms are in red and RuO_6 octahedrons are in blue a) seen from the b direction b) seen from the a direction

a) Structure of $Sr_2Ru_3O_9(OH)$

Around 15 mg of the pure material has been synthetized using the process described in the synthesis part. In a 20 mL Teflon-lined steel autoclave, 15 mg of $KRuO_4$ and 15.6 mg of $Sr(NO_3)_2$ (1:1 molar ratio) are mixed in 5 mL of 0.5 M KOH aqueous solution and heated to 200°C for 72 hours in a preheated chamber furnace. The powder is then washed using the protocol described in the synthesis part. SEM

micrographs show the formation of rhombic platelets (inset of Figure 10). EDX measurements indicate a strontium: ruthenium ratio around 2:3.

Indexation (using DICVOL program) of the powder X-ray diffraction pattern leads to a monoclinic unit cell with the following lattice parameters a = 6.98239(6) Å, b =11.70400(10) Å, c = 9.65014(7) Å and β = 90.7798(11)° (V = 788.55 Å^3), with possible space group $P2_1/c$ or one of its subgroups. The unit cell and stoichiometry shows strong similarities with $Ba_2Ru_3O_9(OH)$, which was reported to crystallize in the orthorhombic $P2_12_12_1$ space group with lattice parameters a = 12.1967 Å, b = 9.8791 Å and c = 7.0616 Å (V= 850.87 Å^3)[10]. This accounts for the smaller ionic radius for Sr compared to Ba. At this stage, two strategies can be followed: the first one consists in starting from the structural model reported for $Ba_2Ru_3O_9(OH)$[10], replace Ba with Sr and decrease the symmetry into a monoclinic subgroup. This would indicate that $Sr_2Ru_3O_9(OH)$ crystallizes in the $P2_1$ space group. The second strategy would be to solve the structure from scratch. For this, a single crystal was peaked and the structural model was solved from single crystal diffraction in the $P2_1/c$ space group. The resulting crystallographic tables are gathered in SI. Using this structural model, the synchrotron x-ray diffraction pattern was refined using the Rietveld method (Figure 10). Both structural models, in $P2_1$ or $P2_1/c$, just differ by the hydrogen positions of the hydroxyl groups which are not accessible from XRD; moreover the highest symmetry ($P2_1/c$) leads to similar reliability factors, whatever for powder or single crystal refinements. As for $Ba_2Ru_3O_9(OH)$, the structure (Figure 11) consists in trimers of edge-sharing RuO_6 octahedra linked together by corners and forming corrugated layers stacked along the c-direction. Strontium atoms are in the interlayer. Note that a bond valence sum analysis (BVS) supports our preliminary localization of hydrogen atoms in the structure because the BVS on both O2 and O4 are closer to -1 rather than -2, which does not come as a surprise since O2 and O4 are the only oxygen atoms not being linked to two ruthenium atoms. However, to confirm the space group assignment and obtain accurate proton positions, neutron diffraction would be highly desirable, provided the synthesis can be scaled up.

To conclude, $Sr_2Ru_3O_9(OH)$ presents a small monoclinic distortion compared to the orthorhombic $Ba_2Ru_3O_9(OH)$. This distortion is due to a slight shift in the stacking of RuO_6 layers, which is made possible by less efficient screening of O layers repulsion by the small Sr ions. Finally using TGA and ex situ XRD diffraction this material is found to decompose around 500°C under argon to form $SrRuO_3$ and RuO_2 (Figure S9).

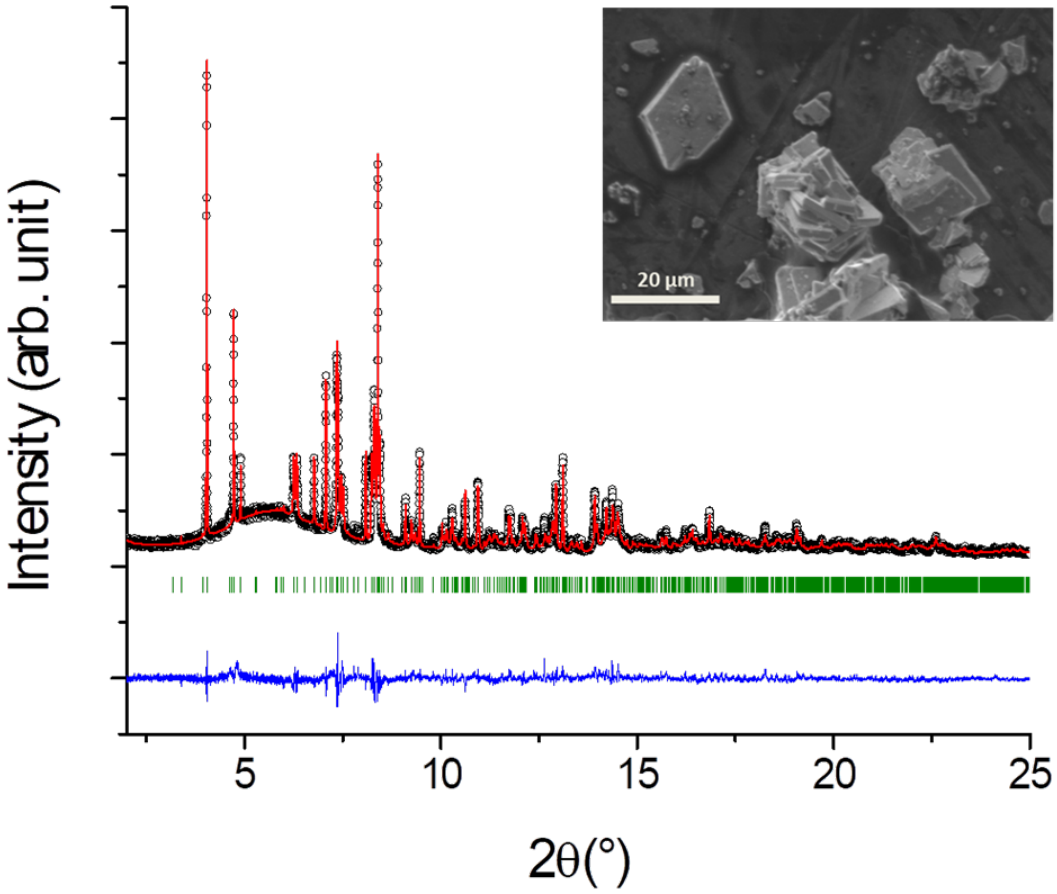

Figure 10: Rietveld refinement of synchrotron X-ray diffraction patterns of $Sr_2Ru_3O_9(OH)$ (λ= 0.412763 Å). The black circles, red continuous line, and bottom blue line represent the observed, calculated, and difference patterns, respectively. Vertical green tick bars are the Bragg positions. Insert: SEM picture of $Sr_2Ru_3O_9(OH)$ crystals

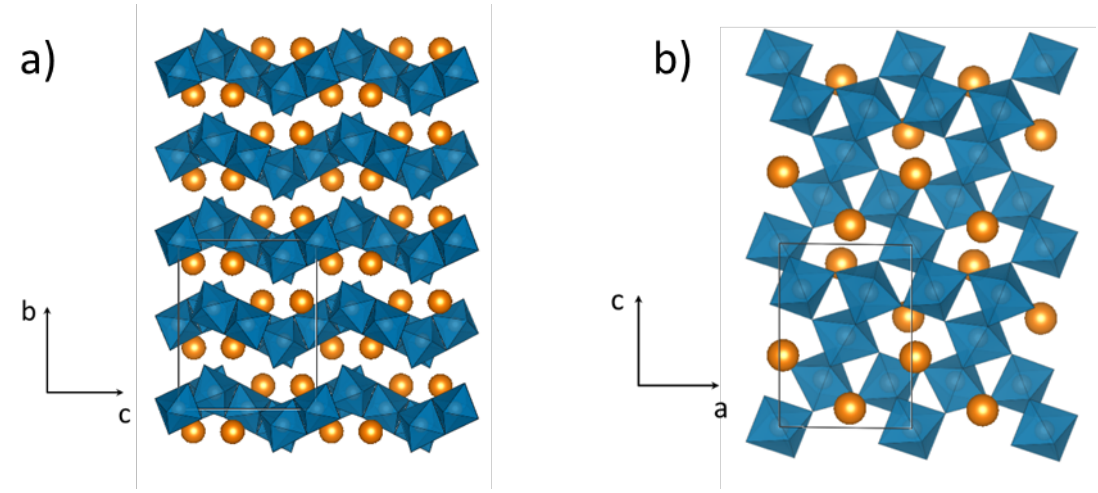

Figure 11: The structure $Sr_2Ru_3O_9(OH)$, Sr atoms are in orange and RuO_6 octahedrons are in blue a) seen from the a direction b) seen from the b direction

d) $BaRu_2O_6$

About 100 mg of pure $BaRu_2O_6$ was obtained by mixing $KRuO_4$ with BaO_2 (2:1 molar ratio) with 1 mL of distilled water in a 10 mL silicon carbide vessel, which was subsequently heated to 200°C in three

minutes and hold at 200°C for three hours in a microwave oven. The obtained powder is then washed using the protocol described in the synthesis part.

The XRD pattern can be indexed using hexagonal space group (with a = 5.2296 Å, c = 11.1752 Å). The material is structurally close to the strontium counterpart $SrRu_2O_6$ and the two materials differ only by the oxygen lattice: the distinct oxygen layers stacking lead to prismatic coordination of barium rather than octahedral coordination for strontium. The high interest for $SrRu_2O_6$ high temperature antiferromagnetism[4,24–27] leads us considering the investigation of the electrochemical and magnetic properties of $BaRu_2O_6$. This study along with further structure description will be described in a forthcoming paper.

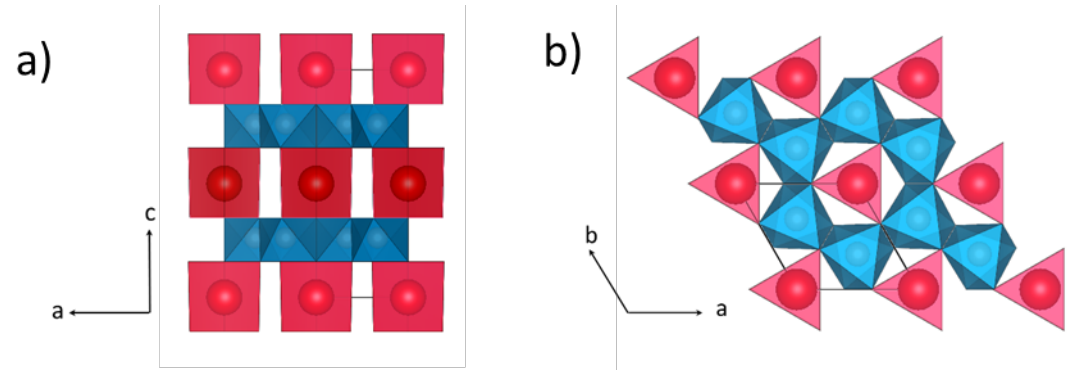

Figure 12: The structure of $BaRu_2O_6$ Ba atoms are in red and RuO_6 octahedrons are in blue a) the layer structure arrangement b) one layer viewed along a direction.

Discussion and conclusion

In this study we have exploited the high versatility of the hydrothermal approach. Using solutions of highly oxidized ruthenate salt ($KRuO_4$) and alkaline-earth salts of barium or strontium and adjusting the pH we have shown that a great diversity of alkaline-earth ruthenates oxides can be synthetized. Five different barium ruthenates ($BaRu_2O_6$, $Ba_2Ru_3O_9(OH)$, $Ba_2Ru_3O_{10}$, $Ba_5Ru_4O_{15}$ and $Ba_4Ru_3O_{10.2}(OH)_{1.8}$) and three strontium ruthenates ($SrRu_2O_6$, $Sr_2Ru_3O_9(OH)$, $Sr_2Ru_3O_{10}$) were obtained, among them **$BaRu_2O_6$, $Ba_2Ru_3O_{10}$, $Ba_5Ru_4O_{15}$** and **$Sr_2Ru_3O_9(OH)$** of different dimensionality are reported here for the first time. All these compounds were found to decompose above 500°C which suggests that they wouldn't be obtained using conventional high temperature approaches. We found the pH to be essential in ruling the reaction pathway with subtle impacts of both reactant ratio and temperature. Moreover, we demonstrated that the counter cation also participates to the reaction as **$NaBa_4Ru_3O_{12}$** and **$LiBa_4Ru_3O_{12}$** were synthetized using LiOH or NaOH as hydroxide source. Furthermore, obviously, in light of this work more compounds await to be discovered.

The effect of reactant ratio as well as the hydroxide concentration can be rationalised regarding the reaction of formation of these compounds. Indeed, the equation shows that the compounds obtained

at higher [HO^-] are stabilised by [HO^-] increase whereas the one formed a lower pH tends to be destabilised. However, this thermodynamic scenario is not able to explain all the experimental observations. Indeed kinetic limitation as to be taken into account as the increase of hydroxide concentration clearly slow down the synthesis reaction. The implication of reaction kinetics in the structural control is likely and the exploration of this point is primordial to extend this work to obtain new materials.

Another attractive feature of these materials is nested in their Ru oxidation state that is equal or greater than 5 as opposed to most of the reported binary or ternary ruthenates. Because of their d^3 and d^2 electronic structure they offer a new ground for attractive physical properties such as the onset of an antiferromagnetic transition temperature T_N as high as 563K[4,24–27]. This was an impetus for investigating the magnetic properties of the Ba analogue as well as of other ruthenates having different dimensionality by modifying the M/Ru ratio (with M=Sr or Ba) as it will be reported in an upcoming paper. Although we limited this report to the Ba and Sr alkaline earth ruthenates we have in parallel demonstrated the feasibility to obtain, by varying the reacting pH, other Ca/Ru compositions besides the single one $Ca_{2-x}Ru_2O_7$ solely reported by Hiley et al[10]. Interestingly, we should recall a similar strategy has previously led to the synthesis of silver based ruthenate phase [12,13]. Thus obvious future investigations could aim in replacing alkaline earth by alkali ions or ruthenium itself by other elements of practical interest, namely Mn. Interestingly, $KMnO_4$ reduction in water has already been used to form manganese oxides[28] and alike $KRuO_4$, $KMnO_4$ can also be thermally reduced by water.

Altogether, these results confirmed the richness of the hydrothermal approach in preparing new metastable phases provided than we identify the reacting pathways and their dependence in governing the nucleation-growth processes of new phases. We hope this work to inspire other groups as numerous metastable materials remain to be isolated by solution chemistry.

Acknowledgement

The authors would like to thank Nicolas Dubouis, Alexis Grimaud, Sathiya Mariyappan for fruitful discussions and Daniel Alves Dalla Corte for is help using MEB. T.M. would like to acknowledge the Ecole Normale Supérieure Paris Saclay for his PhD scholarship. Use of the 11-BM mail service of the APS at Argonne National Laboratory was supported by the US Department of Energy under contract No. DE-AC02-06CH11357 and is gratefully acknowledged. J-M.T. thanks the French National Research Agency for its support to through the Labex STORE-EX project (ANR-10LABX-76-01).

References

(1) Lee, Y.; Suntivich, J.; May, K. J.; Perry, E. E.; Shao-Horn, Y. Synthesis and Activities of Rutile IrO 2 and RuO 2 Nanoparticles for Oxygen Evolution in Acid and Alkaline Solutions. *J. Phys. Chem. Lett.* **2012**, *3* (3), 399–404. https://doi.org/10.1021/jz2016507.

(2) Sathiya, M.; Rousse, G.; Ramesha, K.; Laisa, C. P.; Vezin, H.; Sougrati, M. T.; Doublet, M. L.; Foix, D.; Gonbeau, D.; Walker, W.; et al. Reversible Anionic Redox Chemistry in High-Capacity Layered-Oxide Electrodes. *Nat. Mater.* **2013**, *12* (9), 827–835. https://doi.org/10.1038/nmat3699.

(3) Ishida, K.; Mukuda, H.; Kitaoka, Y.; Asayama, K.; Mao, Z. Q.; Mori, Y.; Maeno, Y. Spin-Triplet Superconductivity in Sr2RuO4 Identified by 17O Knight Shift. *Nature* **1998**, *396* (6712), 658–660. https://doi.org/10.1038/25315.

(4) Hiley, C. I.; Scanlon, D. O.; Sokol, A. A.; Woodley, S. M.; Ganose, A. M.; Sangiao, S.; De Teresa, J. M.; Manuel, P.; Khalyavin, D. D.; Walker, M.; et al. Antiferromagnetism at T>500 K in the Layered Hexagonal Ruthenate SrR U2 O6. *Phys. Rev. B - Condens. Matter Mater. Phys.* **2015**, *92* (10), 1–7. https://doi.org/10.1103/PhysRevB.92.104413.

(5) Jolivet J-P., Henry M., Livage J., and B. E. Metal Oxide Chemistry and Synthesis. 2000, p 318.

(6) Ranade, M. R.; Navrotsky, A.; Zhang, H. Z.; Banfield, J. F.; Elder, S. H.; Zaban, A.; Borse, P. H.; Kulkarni, S. K.; Doran, G. S.; Whitfield, H. J. Energetics of Nanocrystalline TiO2. *Proc. Natl. Acad. Sci.* **2002**, *99* (Supplement 2), 6476–6481. https://doi.org/10.1073/pnas.251534898.

(7) Kitchaev, D. A.; Ceder, G. Evaluating Structure Selection in the Hydrothermal Growth of FeS 2 Pyrite and Marcasite. *Nat. Commun.* **2016**, *7*, 1–7. https://doi.org/10.1038/ncomms13799.

(8) Renard, C.; Abraham, F. High-Pressure Synthesis and Crystal Structure of a New Strontium Ruthenium Oxide : Sr 2 Ru 3 O 10. **1999**, *272*, 266–272.

(9) Munenaka, T.; Sato, H. A Novel Pyrochlore Ruthenate: Ca2Ru2O7. *J. Phys. Soc. Japan* **2006**, *75* (10), 5–8. https://doi.org/10.1143/JPSJ.75.103801.

(10) Hiley, C. I.; Lees, M. R.; Fisher, J. M.; Thompsett, D.; Agrestini, S.; Smith, R. I.; Walton, R. I. Ruthenium(V) Oxides from Low-Temperature Hydrothermal Synthesis. *Angew. Chemie - Int. Ed.* **2014**, *53* (17), 4423–4427. https://doi.org/10.1002/anie.201310110.

(11) Hiley, C. I.; Lees, M. R.; Hammond, D. L.; Kashtiban, R. J.; Sloan, J.; Smith, R. I.; Walton, R. I. Ba $_4$ Ru $_3$ O $_{10.2}$ (OH) $_{1.8}$: A New Member of the Layered Hexagonal Perovskite Family Crystallised from Water. *Chem. Commun.* **2016**, *52* (38), 6375–6378.

https://doi.org/10.1039/C6CC02121B.

(12) Prasad, B. E.; Kazin, P.; Komarek, A. C.; Felser, C.; Jansen, M. β-Ag3RuO4, a Ruthenate(V) Featuring Spin Tetramers on a Two-Dimensional Trigonal Lattice. *Angew. Chemie - Int. Ed.* **2016**, *55* (14), 4467–4471. https://doi.org/10.1002/anie.201510576.

(13) Prasad, B. E.; Kanungo, S.; Jansen, M.; Komarek, A. C.; Yan, B.; Manuel, P.; Felser, C. AgRuO3, a Strongly Exchange-Coupled Honeycomb Compound Lacking Long-Range Magnetic Order. *Chem. - A Eur. J.* **2017**, *23* (19), 4680–4686. https://doi.org/10.1002/chem.201606057.

(14) Rodríguez-Carvajal, J. Recent Advances in Magnetic Structure Determination by Neutron Powder Diffraction. *Phys. B Phys. Condens. Matter* **1993**, *192* (1–2), 55–69. https://doi.org/10.1016/0921-4526(93)90108-I.

(15) Rothkirch, A.; Gatta, G. D.; Meyer, M.; Merkel, S.; Merlini, M.; Liermann, H.-P. Single-Crystal Diffraction at the Extreme Conditions Beamline P02.2: Procedure for Collecting and Analyzing High-Pressure Single-Crystal Data. *J. Synchrotron Radiat.* **2013**, *20* (5), 711–720. https://doi.org/10.1107/s0909049513018621.

(16) Sheldrick, G. M. SHELXT - Integrated Space-Group and Crystal-Structure Determination. *Acta Crystallogr. Sect. A Found. Crystallogr.* **2015**, *71* (1), 3–8. https://doi.org/10.1107/S2053273314026370.

(17) Dolomanov, O. V.; Bourhis, L. J.; Gildea, R. J.; Howard, J. A. K.; Puschmann, H. OLEX2 : A Complete Structure Solution, Refinement and Analysis Program . *J. Appl. Crystallogr.* **2009**, *42* (2), 339–341. https://doi.org/10.1107/s0021889808042726.

(18) Povar, I.; Spinu, O. Ruthenium Redox Equilibria: 3. Pourbaix Diagrams for the Systems Ru-H2O and Ru-Cl--H2O. *J. Electrochem. Sci. Eng.* **2016**, *6* (1), 145. https://doi.org/10.5599/jese.229.

(19) Ogawa, T.; Sato, H. New Ternary Barium Ruthenates: 10H-Type BaRuO3and Ba2Ru7O18. *J. Alloys Compd.* **2004**, *383* (1–2), 313–318. https://doi.org/10.1016/j.jallcom.2004.04.035.

(20) Hong, S.-T.; Sleight, A. W. Crystal Structure of 4H BaRuO 3 : High Pressure Phase Prepared at Ambient Pressure. *J. Solid State Chem.* **1997**, *128* (128), 251–255.

(21) Casas-Cabanas, M.; Reynaud, M.; Rikarte, J.; Horbach, P.; Rodríguez-Carvajal, J. FAULTS : A Program for Refinement of Structures with Extended Defects . *J. Appl. Crystallogr.* **2016**, *49* (6), 2259–2269. https://doi.org/10.1107/s1600576716014473.

(22) Boultif, A.; Loueer, D. Indexing of Powder Diffraction Patterns for Low-Symmetry Lattices by the Successive Dichotomy Method. *J. Appl. Crystallogr.* **1991**, *24* (pt 6), 987–993. https://doi.org/10.1107/S0021889891006441.

(23) Boultif, A. History of the Dichotomy Method for Powder Pattern Indexing. *Powder Diffr.* **2005**, *20* (04), 284–287. https://doi.org/10.1154/1.2135307.

(24) Singh, D. J. Electronic Structure and the Origin of the High Ordering Temperature in SrRu2O6. **2015**, *6056*, 1–4. https://doi.org/10.1103/PhysRevB.91.214420.

(25) Streltsov, S.; Mazin, I. I.; Foyevtsova, K. Localized Itinerant Electrons and Unique Magnetic Properties of SrRu2 O6. *Phys. Rev. B - Condens. Matter Mater. Phys.* **2015**, *92* (13), 1–6. https://doi.org/10.1103/PhysRevB.92.134408.

(26) Tian, W.; Svoboda, C.; Ochi, M.; Matsuda, M.; Cao, H. B.; Cheng, J. G.; Sales, B. C.; Mandrus, D. G.; Arita, R.; Trivedi, N.; et al. High Antiferromagnetic Transition Temperature of the Honeycomb Compound SrRu2 O6. *Phys. Rev. B - Condens. Matter Mater. Phys.* **2015**, *92* (10). https://doi.org/10.1103/PhysRevB.92.100404.

(27) Suzuki, H.; Gretarsson, H.; Ishikawa, H.; Ueda, K.; Yang, Z.; Liu, H.; Kim, H.; Kukusta, D.; Yaresko, A.; Minola, M.; et al. Spin Waves and Spin-State Transitions in a Ruthenate High-Temperature Antiferromagnet. *Nat. Mater.* **2019**. https://doi.org/10.1038/s41563-019-0327-2.

(28) Portehault, D.; Cassaignon, S.; Jolivet, J. Structural and Morphological Control of Manganese Oxide Nanoparticles upon Soft Aqueous Precipitation through MnO 4 À / Mn 2 + Reaction †. **2009**, 2407–2416. https://doi.org/10.1039/b816348k.

$P6_3/mmc$		*R_{Bragg} = 5.2%*	*χ^2 =3.17*			
a = 5.79219(11) Å		*c = 23.53580(15) Å*				*Vol = 683.824 Å³*
Atom	***Wyckoff Position***	***x/a***	***y/a***	***z/a***	***B_{iso} (Å²)***	***Occupancy***
Ru1	2*a*	0	0	0	0.73(4)	0
Ru2	4*e*	0	0	0.09782(10)	0.73(4)	1
Ru3	4*f*	2/3	1/3	0.69426(9)	0.73(4)	1
Ba1	2*b*	0	0	1/4	1.166(19)	1
Ba2	4*f*	2/3	1/3	0.14884(8)	1.166(19)	1
Ba3	4*f*	1/3	2/3	0.04491(7)	1.166(19)	1
O1	6*h*	0.477(2)	0.954(4)	1/4	0.49(8)	1
O2	12*k*	0.1688(15)	0.338(3)	0.1495(3)	0.49(8)	1
O3	12*k*	0.1666(17)	0.333(3)	0.5502(3)	0.49(8)	1

Table 1: Crystallographic data and atomic positions of $Ba_5Ru_4O_{15}$ determined from both Rietveld and corrected by FAULT refinement of its XRD synchrotron pattern.

C2/m			*R_{bragg}= 4.87%*	*χ^2=4.08*		
a= 11.45981(1) Å	*b= 5.80123(1) Å*	*c= 6.50787(1) Å*		*β= 104.9487(1) °*		*Vol= 418.008 Å³*
Atom	***Wyckoff Position***	***x/a***	***y/a***	***z/a***	***B_{iso} (Å²)***	***Occupancy***
Ru1	2*a*	0	0	0	0.109 (11)	1
Ru2	4*h*	0	0.23634(9)	1/2	0.109(11)	1
Ba1	4i	0.67499(3)	0	0.14776(5)	0.971(5)	1
O1	8*j*	0.9797(2)	0.2390(4)	0.1930(3)	0.95(3)	1
O2	4*i*	0.1776(3)	0	0.1339(5)	0.95(3)	1
O3	4*i*	0.3937(3)	0	0.4745(5)	0.95(3)	1
O4	4*i*	0.8778(3)	0	0.4833(5)	0.95(3)	1

Table 2: Crystallographic data and atomic positions of $Ba_2Ru_3O_{10}$ determined from Rietveld refinement of its XRD synchrotron pattern

$P2_1/c$		R_{Bragg} = 6.65%	χ^2=1.68			
a= 6.98239 (6) Å	b=11.70400 (10) Å	c= 9.65014 (7) Å	β=90.7798°(11)			Vol= 788.552 Å³
Atom	**Wyckoff Position**	**x/a**	**y/a**	**z/a**	**B_{iso} (Å²)**	**Occupancy**
Sr1	4*e*	0.9747(6)	0.3642(5)	0.1113(6)	3.62(7)	1
Sr2	4*e*	0.4709(6)	0.1355(5)	0.8953(5)	3.62(7)	1
Ru1	4*e*	0.1713(6)	0.5971(3)	0.2527(5)	0.873(18)	1
Ru2	4*e*	0.3231(6)	0.4061(3)	0.7604(5)	0.873(18)	1
Ru3	2*a*	0	1/2	1/2	0.873(18)	1
Ru4	2*d*	½	1/2	0	0.873(18)	1
O1	4*e*	0.961(3)	0.6284(16)	0.134(2)	0.021(14)	1
O2	4*e*	0.423(3)	0.2382(15)	0.7011(19)	0.021(14)	1
O3	4*e*	0.747(3)	0.5450(17)	0.403(2)	0.021(14)	1
O4	4*e*	0.241(3)	0.7495(18)	0.1429(19)	0.021(14)	1
O5	4*e*	0.187(3)	0.4438(18)	0.329(2)	0.021(14)	1
O6	4*e*	0.338(3)	0.5644(18)	0.826(2)	0.021(14)	1
O7	4*e*	0.417(3)	0.3382(18)	0.938(2)	0.021(14)	1
O8	4*e*	0.903(3)	0.3355(19)	0.560(2)	0.021(14)	1
O9	4*e*	0.242(3)	0.5163(19)	0.097(2)	0.021(14)	1
O10	4*e*	0.428(3)	0.5891(17)	0.344(2)	0.021(14)	1

Table 3: Crystallographic data and atomic positions of $Sr_2Ru_3O_9(OH)$ determined from Rietveld refinement of its XRD synchrotron pattern

Supplementary Information

Elemental Analysis

The atomic ratio of Ru/M (where M=Sr/Ba) where determined using energy dispersive X-ray spectrometry (EDX) and are reported in table. ICP-Ms analysis attempts were done to determine the stoichiometry of the compounds, but the phases described above where found to form RuO_2 after acidic treatment (aqua regia or HCL 37%), . RuO_2 is insoluble in acidic media and then the analyses was not convincing.

Phase	Theoretical Ru/M (M= Ba, Sr)	Experimental Ru/M
$Ba_5Ru_4O_{15}$	0.8	0.9(0.1)
$Ba_2Ru_3O_{10}$	1.5	1.4 (0.1)
$BaRu_2O_6$	2	1.9 (0.1)
$Sr_2Ru_3O_9(OH)$	1.5	1.6 (0.1)
$Sr_2Ru_3O_{10}$	1.5	1.7 (0.1)

$Sr_2Ru_3O_{10}$

In a 20 mL Teflon-lined steel autoclave, 200 mg of $KRuO_4$, 207.3 mg of Sr(NO3)2((1:1 molar ratio) are mixed in 10 mL of 3M KOH aqueous solution and heated to 200°C in a preheated fan oven for 72 hours. The powder is then washed using the protocol described in the synthesis part. SEM micrographs show the formation of rectangular facetted micrometer-sized platelets (Figure 6). The synchrotron x-ray pattern was refined using previous work structural model. The structural datas can be found in the table

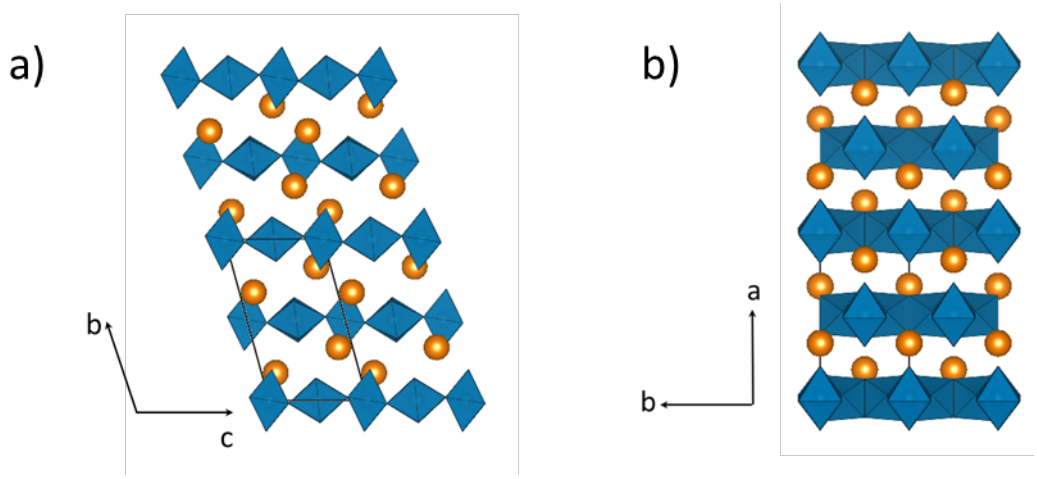

Figure S1 : The structure of $Sr_2Ru_3O_{10}$, Sr atoms are in red and RuO_6 octahedrons are in blue a) seen from the a direction b) seen from the c direction

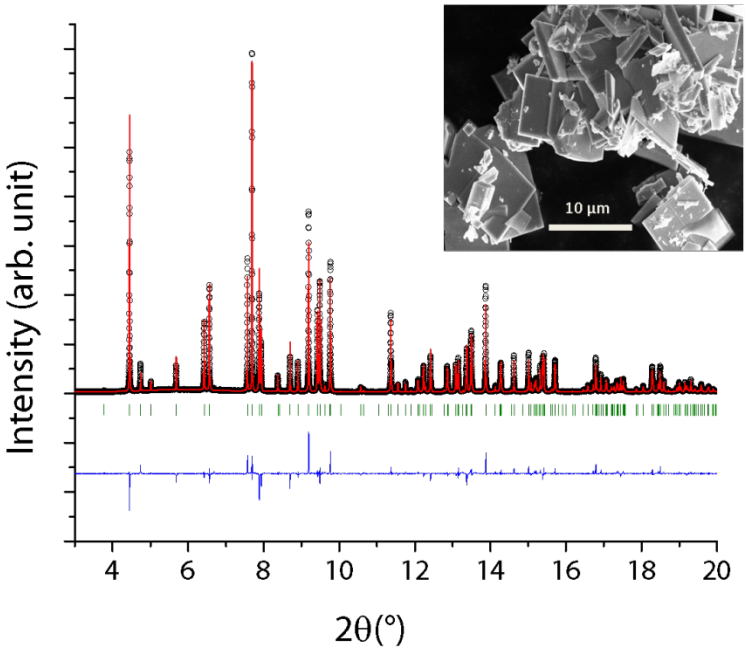

Figure S 2 : Rietveld refinement of synchrotron and neutron diffraction patterns of $Sr_2Ru_3O_{10}$. The black circles, red continuous line, and bottom blue line represent the observed, calculated, and difference patterns, respectively. Vertical green tick bars are the Bragg positions. Insert: SEM picture of $Sr_2Ru_3O_{10}$ crystals

C2/m		*R_{Bragg} = 5.38%*		*χ^2 = 3.88*		
a= 11.03163(2) Å	*b= 5.65362(0) Å*	*c= 6.48815(0) Å*		*β=105,4421(0)°*		*Vol=390.049 Å³*
Atom	***Wyckoff Position***	***x/a***	***y/a***	***z/a***	***B_{iso} (Å²)***	***Occupancy***
Ru1	2*a*	0	0	0	0.353(5)	1
Ru2	4*h*	0	0.23237(11)	1/2	0.353(5)	1
Sr1	4*i*	0.67113(5)	0	0.14399(9)	0.125(6)	1
O1	8*j*	0.9782(2)	0.2417(5)	0.1871(4)	0.94(3)	1
O2	4*i*	0.1924(3)	0	0.1176(5)	0.94(3)	1
O3	4*i*	0.3759(4)	0	0.4703(6)	0.94(3)	1
O4	4*i*	0.8624(3)	0	0.4614(6)	0.94(3)	1

Table S 1 : Crystallographic data and atomic positions of $Sr_2Ru_3O_{10}$ determined from Rietveld refinement of its XRD synchrotron pattern

$Ba_5Ru_4O_{15}$

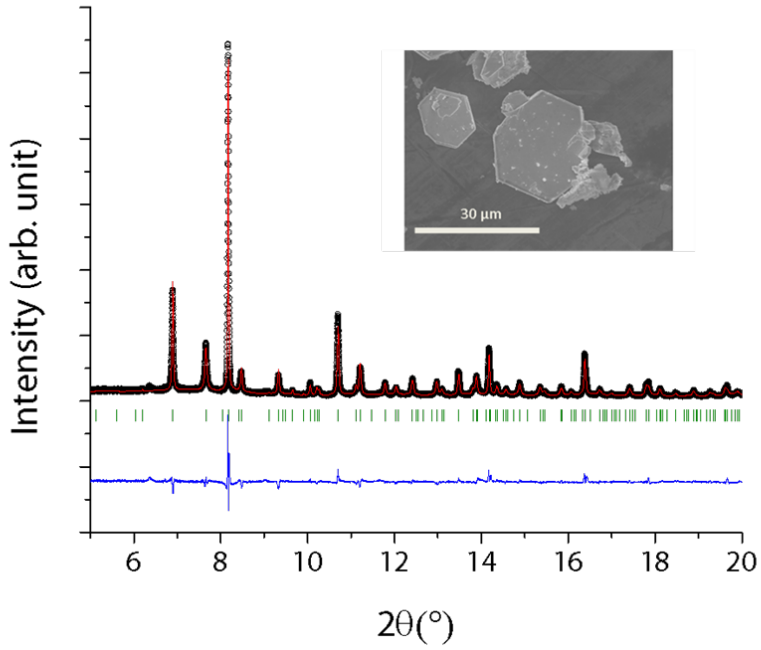

Figure S3 : Rietveld refinement of synchrotron X-ray diffraction patterns of Ba5Ru4O15 (λ= 0.412763 Å). The black circles, red continuous line, and bottom blue line represent the observed, calculated, and difference patterns, respectively. Vertical green tick bars are the Bragg positions. Insert: SEM picture of Ba5Ru4O15 crystals

$P6_3/mmc$			R_{Bragg} **= 5.2%**	χ^2 **=3.17**		
a = 5.79219(11) Å		***c = 23.53580(15) Å***				***Vol = 683.824 Å³***
Atom	***Wyckoff Position***	***x/a***	***y/a***	***z/a***	***B_{iso} (Å²)***	***Occupancy***
Ru1	2*a*	0	0	0	0.73 (4)	0.4
Ru2	4*e*	0	0	0.09782(10)	0.73 (4)	1
Ru3	4*f*	2/3	1/3	0.69426 (9)	0.73 (4)	1
Ba1	2*b*	0	0	1/4	1.166(19)	1
Ba2	4*f*	2/3	1/3	0.14884(8)	1.166(19)	1
Ba3	4*f*	1/3	2/3	0.04491(7)	1.166(19)	1
O1	6*h*	0.477(2)	0.954(4)	1/4	0.49(8)	1
O2	12*k*	0.1688(15)	0.338(3)	0.1495 (3)	0.49(8)	1
O3	12*k*	0.1666 (17)	0.333(3)	0.5502 (3)	0.49(8)	1

Table S2 : Crystallographic data and atomic positions of $Ba_5Ru_4O_{15}$ determined from Rietveld refinement of its XRD synchrotron pattern

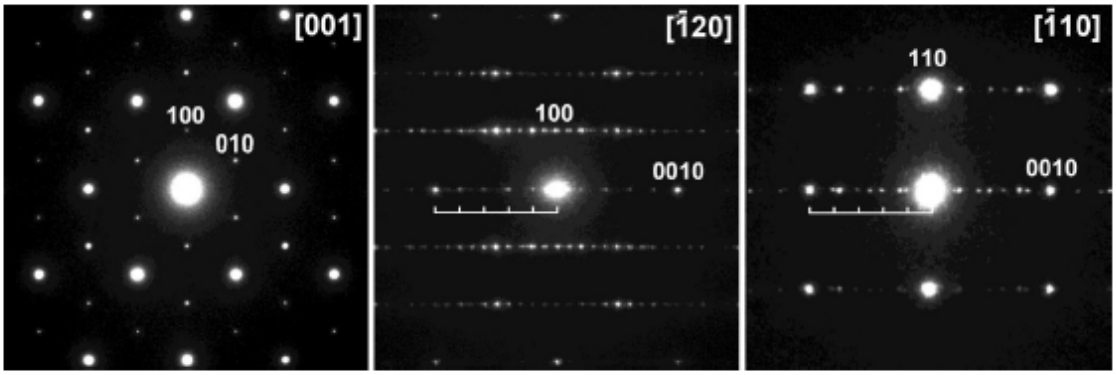

Figure S4 : ED patterns of $Ba_5Ru_4O_{15}$. The brackets mark reflections from 10H-$Ba_5Ru_4O_{15}$

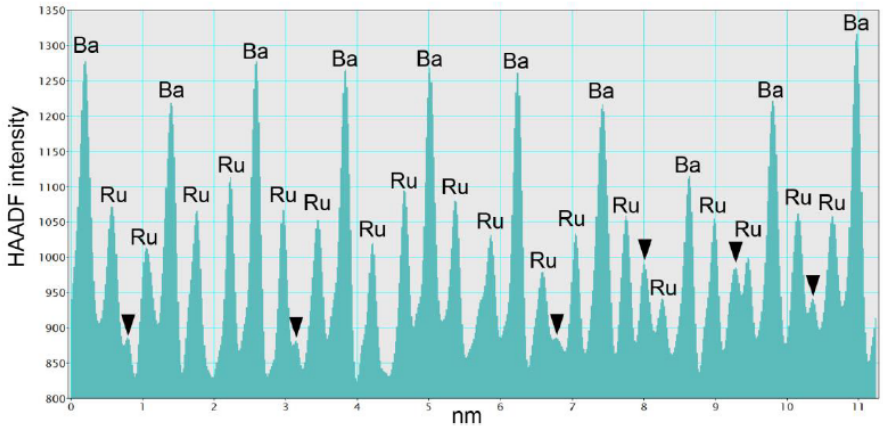

Figure S5 : HAADF intensity profile along the triple octahedral chains. Note variable intensity at the place of the mid octahedron (black arrowheads) indicating its random population with Ru cation and vacancy. The Ru cations are randomly shifted from the centers of these mid octahedra

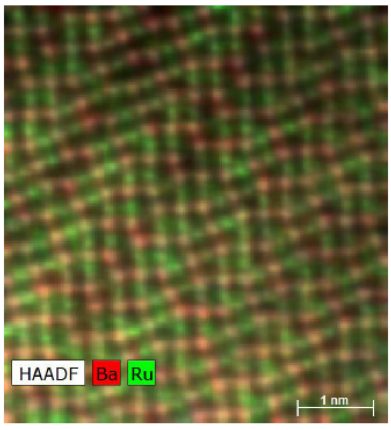

Figure S6 : Atomic resolution EDX map of the interface between 4H-BaRuO3 and 10H-Ba5Ru4O15 (going from top right corner to the left bottom corner)

Thermal stability

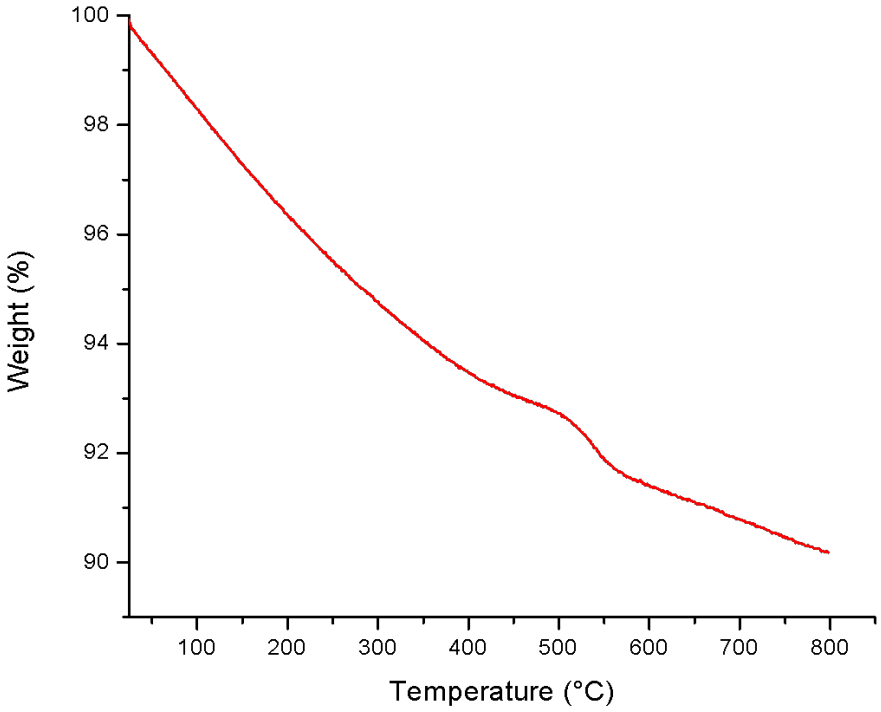

Figure S7 : TGA of $Ba_5Ru_4O_{15}$ under argon.

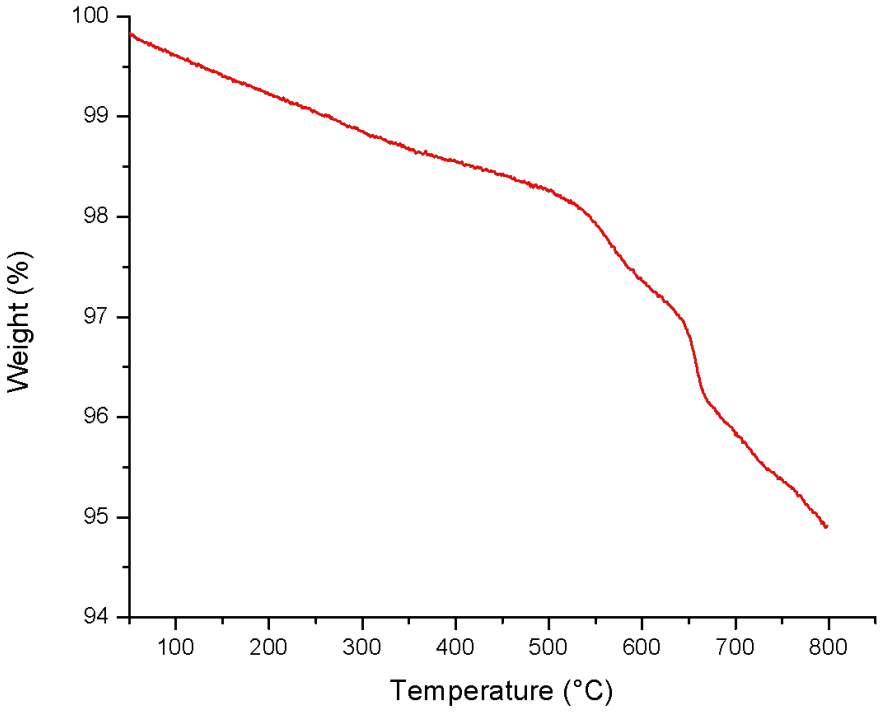

Figure S8: TGA of $Ba_2Ru_3O_{10}$ under argon

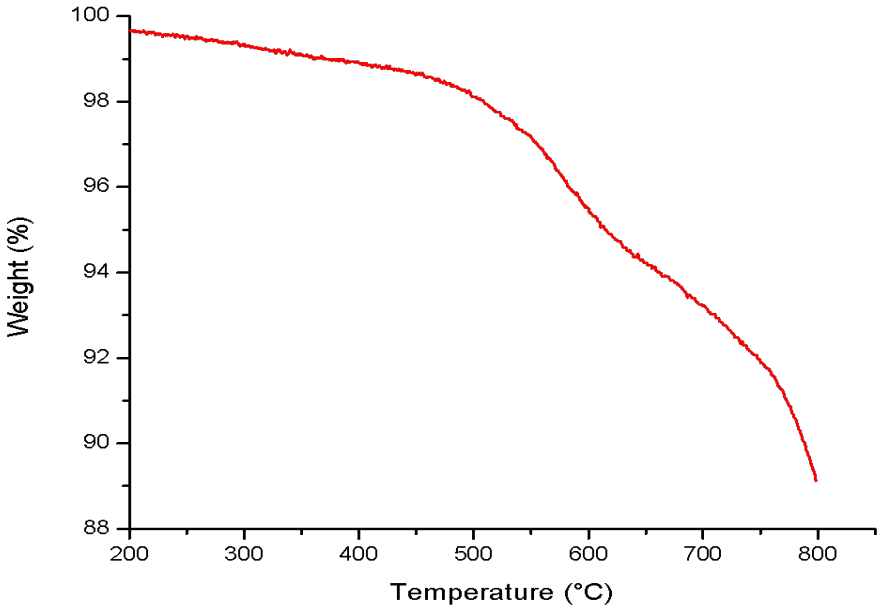

Figure S9 : TGA of $Sr_2Ru_3O_9(OH)$ under argon

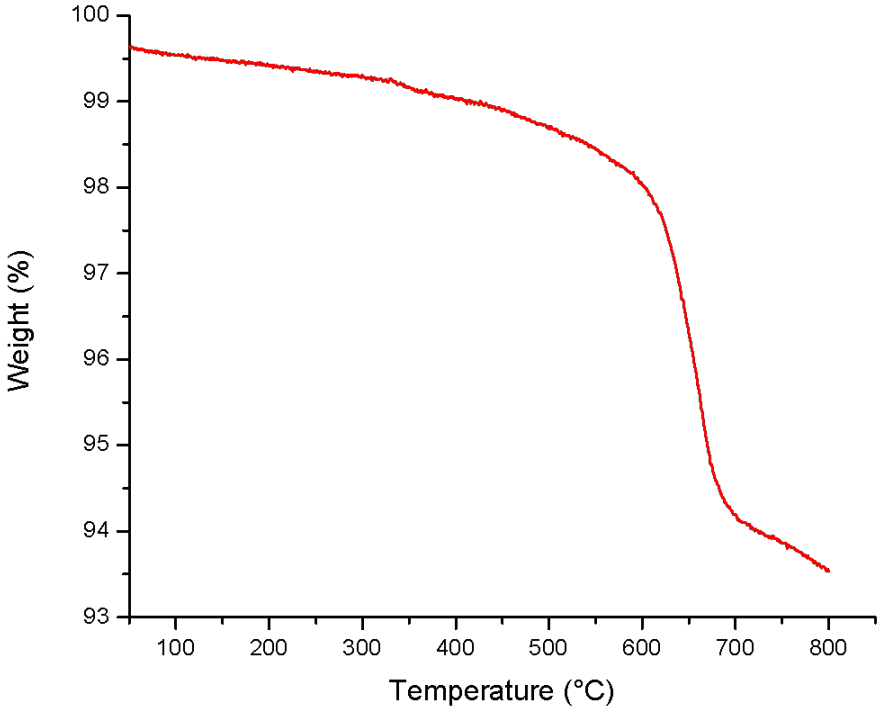

Figure S10: TGA $Sr_2Ru_3O_{10}$ under argon

Monocristal datas

Empirical formula	$Sr_2Ru_3O_9(OH)$
Formula weight	639.45
Temperature/K	293(2)
Crystal system	monoclinic
Space group	$P2_1/c$
a/Å	6.9744(6)
b/Å	11.7100(10)
c/Å	9.6524(12)
α/°	90
β/°	90.084(11)
γ/°	90
Volume/Å^3	788.31(14)
Z	2
ρ_{calc}g/cm^3	5.387
μ/mm^{-1}	19.102
F(000)	1152.0
Crystal size/mm^3	0.02 × 0.02 × 0.02
Radiation	MoKα (λ = 0.71073)
2Θ range for data collection/°	5.47 to 52.742
Index ranges	-8 ≤ h ≤ 8, -14 ≤ k ≤ 14, -12 ≤ l ≤ 11
Reflections collected	5625
Independent reflections	1603 [R_{int} = 0.0457, R_{sigma} = 0.0378]
Data/restraints/parameters	1603/0/121
Goodness-of-fit on F^2	1.301
Final R indexes [I>=2σ (I)]	R_1 = 0.0613, wR_2 = 0.1684
Final R indexes [all data]	R_1 = 0.0646, wR_2 = 0.1707
Largest diff. peak/hole / e Å^{-3}	2.68/-1.72

Table S3 : Crystal data and structure refinement for $Sr_2Ru_3O_9(OH)$

Atom	*x*	*y*	*z*	U(eq)
Sr1	0.9715(2)	0.36614(13)	0.10717(16)	15.1(4)
Sr2	0.4714(2)	0.13401(13)	0.89307(16)	15.4(4)
Ru1	0.17098(16)	0.59630(10)	0.25605(14)	12.8(3)
Ru2	0.32876(17)	0.40369(10)	0.75744(14)	12.6(3)
Ru3	0	0.5	0.5	14.3(4)
Ru4	0.5	0.5	0	14.2(4)
O1	0.9252(15)	0.5985(9)	0.1636(12)	14.5(16)
O2	0.2876(17)	0.2427(9)	0.6905(12)	16.3(16)
O3	0.7506(14)	0.5250(10)	0.4165(11)	14.9(16)
O4	0.2136(15)	0.7581(10)	0.1914(13)	21(3)
O5	0.1159(14)	0.4429(10)	0.3286(11)	16(2)
O6	0.3860(16)	0.5569(9)	0.8290(11)	16.3(16)
O7	0.4236(14)	0.3465(10)	0.9373(11)	14.9(16)
O8	0.9249(15)	0.3477(10)	0.5645(12)	16(2)
O9	0.2495(14)	0.5258(9)	0.0844(12)	14.5(16)
O10	0.4255(15)	0.5980(10)	0.3376(11)	15(2)

Table S4: Fractional Atomic Coordinates (×104) and Equivalent Isotropic Displacement Parameters (Å2×103) for $Sr_2Ru_3O_9(OH)$. Ueq is defined as 1/3 of the trace of the orthogonalised UIJ tensor.

Atom	U_{11}	U_{22}	U_{33}	U_{23}	U_{13}	U_{12}
Ru01	5.4(6)	10.2(6)	22.7(7)	-2.8(5)	-2.9(5)	1.3(4)
Ru02	6.6(6)	10.2(6)	21.0(7)	2.5(5)	-1.2(5)	0.7(4)
Ru03	11.0(8)	9.8(9)	22.1(9)	-2.5(7)	-6.0(7)	4.3(6)
Ru04	10.8(8)	10.7(9)	21.3(9)	4.3(7)	2.4(7)	3.3(6)
Sr01	13.9(7)	10.5(7)	20.9(8)	0.0(5)	-4.2(5)	-1.8(5)
Sr02	14.1(7)	11.9(7)	20.1(8)	0.8(5)	0.0(6)	2.3(5)
O001	7(4)	9(4)	28(4)	-3(3)	3(3)	4(3)
O002	25(4)	3(3)	21(4)	-2(3)	1(3)	-5(3)
O003	6(3)	21(4)	19(4)	-4(3)	-9(3)	-1(3)
O004	5(5)	21(6)	37(7)	2(5)	-3(4)	-4(4)
O005	5(5)	25(6)	17(5)	-2(5)	-6(4)	-2(4)
O006	25(4)	3(3)	21(4)	-2(3)	1(3)	-5(3)
O007	6(3)	21(4)	19(4)	-4(3)	-9(3)	-1(3)
O008	8(5)	19(6)	22(6)	2(5)	-3(4)	5(4)
O009	7(4)	9(4)	28(4)	-3(3)	3(3)	4(3)
O010	5(5)	29(6)	11(5)	0(4)	-2(4)	2(4)

Table S5: Anisotropic Displacement Parameters ($Å^2 \times 10^3$) for $Sr_4Ru_6O_{20}$. The Anisotropic displacement factor exponent takes the form: $-2\pi^2[h^2a^{*2}U_{11}+2hka^*b^*U_{12}+\ldots]$.